Atmos. Meas. Tech. Discuss., https://doi.org/10.5194/amt-2017-251
Manuscript under review for journal Atmos. Meas. Tech.
Discussion started: 7 August 2017

Atmospheric Measurement Techniques
Discussions

GOCI Yonsei aerosol retrieval version 2 aerosol products: improved algorithm description and error analysis with uncertainty estimation from 5-year validation over East Asia

Myungje Choi[1], Jhoon Kim[1, 2], Jaehwa Lee[3, 4], Mijin Kim[1], Young-Je Park[5], Brent Holben[4], Thomas F. Eck[4, 6], Zhengqiang Li[7], Chul H. Song[8]

[1]Department of Atmospheric Sciences, Yonsei University, Seoul, Republic of Korea
[2]Harvard-Smithsonian Center for Astrophysics, Cambridge, MA, USA
[3]Earth System Science Interdisciplinary Center, University of Maryland, College Park, MD, USA
[4]NASA Goddard Space Flight Center, Greenbelt, MD, USA
[5]Korea Ocean Satellite Center, Korea Institute of Ocean Science and Technology, Ansan, Republic of Korea
[6]Universities Space Research Association, Columbia, MD, USA
[7]State Environmental Protection Key Laboratory of Satellite Remote Sensing, Institute of Remote Sensing and Digital Earth, Chinese Academy of Sciences, Beijing, China
[8]School of Environmental Science and Engineering, Gwangju Institute of Science and Technology (GIST), Gwangju, Republic of Korea

Correspondence to: Jhoon Kim (jkim2@yonsei.ac.kr)

Abstract. The Geostationary Ocean Color Imager (GOCI) Yonsei aerosol retrieval (YAER) version 1 algorithm was developed for retrieving hourly aerosol optical depth at 550 nm (AOD) and other subsidiary aerosol optical properties over East Asia. The GOCI YAER AOD showed comparable accuracy compared to ground-based and other satellite-based observations, but still had errors due to uncertainties in surface reflectance and simple cloud masking. Also, it was not capable of near-real-time (NRT) processing because it required a monthly database of each year encompassing the day of retrieval for the determination of surface reflectance. This study describes the improvement of GOCI YAER algorithm to the version 2 (V2) for NRT processing with improved accuracy from the modification of cloud masking, surface reflectance determination using multi-year Rayleigh corrected reflectance and wind speed database, and inversion channels per surface conditions. Therefore, the improved GOCI AOD (τ_G) is similar with those of Moderate Resolution Imaging Spectroradiometer (MODIS) and Visible Infrared Imaging Radiometer Suite (VIIRS) AOD compared to V1 of the YAER algorithm. The τ_G shows reduced median bias and increased ratio within $0.15\tau_A + 0.05$ range (i.e. absolute expected error range of MODIS AOD) compared to V1 in the validation results using Aerosol Robotic Network (AERONET) AOD (τ_A) from 2011 to 2016. The validation using the Sun-Sky Radiometer Observation Network (SONET) over China also shows similar results. The bias of error ($\tau_G - \tau_A$) is within −0.1 and 0.1 range as a function of AERONET AOD and AE, scattering angle, NDVI, cloud fraction and homogeneity of retrieved AOD, observation time, month, and year. Also, the diagnostic and prognostic expected error (DEE and PEE, respectively) of τ_G are estimated. The estimated multiple PEE of GOCI V2 AOD

Atmos. Meas. Tech. Discuss., https://doi.org/10.5194/amt-2017-251
Manuscript under review for journal Atmos. Meas. Tech.
Discussion started: 7 August 2017

is well matched with actual error over East Asia, and the GOCI V2 AOD over Korea shows higher ratio within PEE compared to over China and Japan.

1 Introduction

Aerosols are one of the most important components in the atmosphere with respect to climate change and air pollution. In respect to climate change, aerosols influence climate directly by scattering and absorbing solar radiance (aerosol-radiation interaction) and indirectly by altering cloud properties (aerosol-cloud interaction) (IPCC, 2013). In terms of aerosol optical properties (AOPs), the aerosol optical depth, single scattering albedo, and surface albedo determine the sign and magnitude of shortwave aerosol radiative forcing of atmosphere (Takemura et al., 2002), thus accurate AOPs retrieval is important to quantify a role of aerosols on climate change. In respect to air pollution, aerosol is a major environment-related threat to human health particularly for the elderly and the young. It affects the both the respiratory and pulmonary systems, resulting in increased incidence of heart disease, stroke, and lung cancer (Lim et al., 2012). The PM consists mainly of a complex mixture components of sulfates, nitrates, ammonia, sodium chloride, black carbon, mineral dust and water (WHO, 2016), and its health impact differs per chemical composition (e.g. Harrison and Yin (2000)). Despite the fact that accurate information of PM is often obtained from the ground-based in-situ measurements, the coverage of ground-based measurements is limited to local scales and the observation network may be sparse, especially in developing countries. On the other hand, the satellite-based remote sensing can provide aerosol information over a much broader area. Although chemical transports models (CTMs) require many assumptions to predict PM concentrations, the accuracy in modeling can be improved significantly through data assimilation with satellite-retrieved AOD products (van Donkelaar et al., 2010).

East Asia is the one of regions where the aerosol concentration is highest in the world and aerosol type is also complicated by components such as desert dust, anthropogenic carbonaceous aerosols, and sea salt (Kim et al., 2007; Yoon et al., 2014). Its trend doesn't show significant decrease as in Europe or North America (Hsu et al., 2012; Zhang and Reid, 2010), and our understanding for aerosol trend is still insufficient (IPCC, 2013).

The Geostationary Ocean Color Imager (GOCI), launched in 2010 as the first ocean color imager in geostationary orbit (GEO), observes East Asia eight times per day from 00:30 to 07:30 Coordinated Universal Time (UTC) (i.e. 09:30 to 16:30 Korea Standard Time (KST)) (Choi et al., 2012). Using the radiance measurements in eight spectral channels (412, 443, 490, 555, 660, 680, 745, and 865 nm) in high spatial resolution of 500 m × 500 m, the GOCI Yonsei aerosol retrieval (YAER) version 1 (V1) algorithm was developed for retrieving hourly aerosol optical properties such as aerosol optical depth (AOD), fine-mode fraction, Ångström exponent and single-scattering albedo (Choi et al., 2016). Because it has more channels with higher spatial resolution in visible and near infrared (NIR) compared to recent and planned advanced meteorological sensors in GEO such as Advanced Himawari Imager (AHI), Advanced Baseline Imager (ABI) and Advanced Meteorological Imager (AMI), these accurate retrievals of AOPs from GOCI provide significant information. Hourly AOD from the GOCI YAER algorithm shows high accuracy with Moderate Resolution Imaging Spectroradiometer (MODIS) and Visible Infrared

Imaging Radiometer Suite (VIIRS) over East Asia (Xiao et al., 2016). The application of GOCI retrievals thus results in the improved performance of several air quality forecasting models to predict AOD and PM concentrations through data assimilation (Jeon et al., 2016; Lee et al., 2017; Lee et al., 2016; Park et al., 2014; Saide et al., 2014). For that reason, the request for GOCI aerosol retrievals with near-real-time (NRT) processing continues for implementing operational air quality forecasting systems with data assimilation.

Lack of shortwave infrared (SWIR) channels in GOCI such as 1.6 or 2.1 μm of MODIS does not allow for the application of method to obtain surface reflectance in visible from the TOA reflectance of SWIR channels (Kaufman et al., 1997). Instead, the minimum reflectivity technique using the composite method (Herman and Celarier, 1997; Hsu et al., 2004; Koelemeijer et al., 2003) was applied in the GOCI YAER V1 algorithm. However due to this methodology, the GOCI YAER V1 algorithm was not capable of near-real-time (NRT) processing because it required a monthly database for each year encompassing the day of retrieval for the determination of surface reflectance. Also, the resulting retrievals showed slightly negative bias over land and positive bias over ocean due to surface reflectance errors, as compared to AERONET data during the Distributed Regional Aerosol Gridded Observation Networks - North East Asia 2012 campaign (DRAGON-NE Asia 2012 campaign) (Choi et al., 2016).

In this study, therefore, the algorithm is improved to “version 2” (V2) not only for NRT processing but also for better accuracy. Monthly and hourly surface reflectance and wind speed determination are modified utilizing a climatological database from the multi-year GOCI dataset and reanalysis wind speed data, respectively. Especially, the surface reflectance database obtained from multi-year Rayleigh corrected reflectance (RCR) samples enables more accurate surface reflectance retrieval by increasing the possibility to select less aerosol and cloud contaminated cases compared to one year samples of the V1 algorithm. The cloud masking and inversion spectral channels for aerosol retrievals were also modified for better accuracy. Furthermore, retrieved GOCI YAER V2 AOD is evaluated using ground-based observation data, along with the comparisons to both the V1 and MODIS retrievals from March 2011 to February 2016, which is longer period evaluation interval compared to previous studies. Also, the bias of the GOCI YAER V2 AOD is analyzed and uncertainty is estimated for better application of GOCI AOD in data assimilation.

In section 2, the improvements of the GOCI YAER V2 algorithm are summarized and quantitative comparison with other satellite AODs are presented. In Section 3, the GOCI YAER V2 AOD is validated using ground-based sunphotometer observations and also with other satellite AODs. In Section 4, the error of GOCI YAER V2 AOD is analyzed according to various parameters and expected error is estimated. Section 5 provides a summary and conclusions.

2 GOCI Yonsei aerosol retrieval version 2 algorithm

2.1 Brief description of GOCI YAER version 1 and V2 algorithm framework

A prototype of the GOCI Yonsei aerosol retrieval (YAER) over ocean (Lee et al., 2010) was developed using MODIS Level 1B (L1B) Top-of-Atmosphere (TOA) reflected radiance data, and improved by using non-spherical aerosol optical properties

Atmos. Meas. Tech. Discuss., https://doi.org/10.5194/amt-2017-251
Manuscript under review for journal Atmos. Meas. Tech.
Discussion started: 7 August 2017

(Lee et al., 2012). Furthermore, using real GOCI L1B TOA radiance data, the GOCI YAER V1 algorithm over land and ocean was developed (Choi et al., 2016). The algorithm is applied to cloud-free and snow/ice-free pixels, so 12 × 12 L1B pixels are aggregated to 6 × 6 km^2 spatial resolution average after cloud/snow/ice masking and suitable pixel selection. Unified aerosol models over land and ocean consist of multi-dimensional categories of aerosol optical properties which are aerosol optical depth (AOD), fine-mode fraction (FMF), and single scattering albedo (SSA) derived from the global Aerosol Robotic Network (AERONET) Inversion database (Dubovik and King, 2000; Holben et al., 1998). The non-spherical properties are considered using the phase function derived from the AERONET data (https://aeronet.gsfc.nasa.gov/). Dark ocean surface reflectance is calculated using the Cox-Munk model (Cox and Munk, 1954) considering Fresnel reflectance with a bidirectional reflectance distribution function according to geometry and wind speed in a pre-calculated Look-up table (LUT) with temporal interpolation of ECMWF wind speed data at 10 m above sea level over dark ocean pixels. Land surface reflectance is obtained by using the minimum reflectivity technique for each month, channel, and hour, and temporal interpolation is carried out over land, turbid ocean, and heavy aerosol pixels in the inversion step. In the algorithm, turbid water pixel detection is implemented using a difference of 660 nm TOA reflectance between directly-observed and interpolated from 412 and 865 nm (hereafter, $\Delta\rho_{660}$) (Choi et al., 2016; Li et al., 2003). All eight channels are used over ocean, and different channels according to surface condition are used over land. The algorithm determines AOD at 550 nm with aerosol models that have the least difference between pre-calculated and observed TOA reflectance in the selected channels. From the selected models, Ångström exponent between 440 and 870 nm (AE), FMF at 550 nm, and SSA at 440 nm are determined together with AOD at 550 nm. Note that a discrete ordinate radiative transfer (DISORT) code of the "libRadtran" software package is used to calculate TOA reflectances for LUT construction based on scalar calculation (i.e. intensity only) and plane-parallel atmosphere approximation (Mayer and Kylling, 2005).

For the better accuracy of aerosol optical properties of GOCI, especially in AOD, the new V2 algorithm is refined piecemeal while retaining the main V1 algorithm concepts. A flowchart of the GOCI YAER V2 algorithm is described in Figure 1. The improved parts of the V2 algorithm compared to V1 are the pixel masking and aggregation procedure, implementation of climatological surface reflectance and wind speed from a 5-year climatological database for NRT capability, turbid water detection, and inversion condition according to land, turbid water, and dark ocean pixels, respectively. The aerosol model construction and inversion method of converting TOA reflectance to aerosol products are identical with those of V1. Therefore, details of refined parts of the algorithm are introduced hereafter.

2.2 Pixel masking and aggregation procedure

The GOCI YAER algorithm is targeted to cloud-free and snow-free pixels over land and cloud-free, ice-free, and high turbidity water free pixels over ocean, therefore several masking steps are required. The previous V1 algorithm contains simple cloud masking techniques, which are a spatial variability test using the standard deviation of 3 × 3 pixels and a high TOA reflectance test using a threshold. As a result, most of cloud pixels are removed well, but there are still some remaining thin homogeneous cloud pixels such as cirrus cloud due to the absence of ice crystal sensitive 1.38 µm or other infra-red channels in GOCI. This could lead to misidentification of remaining cloud contamination as high AOD, and result in the requirement of additional filtering for successful data assimilation between models and GOCI AOD (Xu et al., 2015). It could also lead to inappropriate determination of some low AOD pixels as cloud in regions where there is highly inhomogeneous surface reflectance. In this study, therefore, refined cloud masking techniques are applied and summarized with references in Table 1. Most of these masking techniques were adopted from the MODIS and VIIRS aerosol retrieval and cloud masking algorithms. The masking procedures consist of three stages: masking in 0.5×0.5 km^2 original L1B pixel resolution level, aggregation from 0.5×0.5 km^2 to 6×6 km^2 resolution, and additional masking in 6×6 km^2 resolution level.

In the level of 0.5×0.5 km^2 resolution, the cloud masking over ocean is not changed, but land cloud masking steps are refined. The previous standard deviation (hereafter, "*Stddev*") test of the 3×3 pixels over land for classifying cloud and aerosol (Step 3 in Table 1 except for a threshold of 0.0025) works well in moderate and high AOD cases, but it showed excessive masking over heterogeneous surface reflectance pixels in low AOD condition. Thus, the threshold is relaxed to 0.015, and mean-weighted *Stddev* test (Step 4 in Table 1) and a ratio of maximum and minimum TOA reflectance at 412 nm within 3×3 pixels are adopted (Step 2 in Table 1) as an alternative. To distinguish aerosol and cloud using a different reflectance ratio between 865 and 660 nm, a pseudo Global Environment Monitoring Index (pseudo GEMI), defined in Pinty and Verstraete (1992) and Kopp et al. (2014), is adopted (Step 6 in Table 1). Also, inland water pixels are filtered out using a normalized difference vegetation index (NDVI) calculated using TOA reflectance at 660 and 865 nm (Step 7 in Table 1). A dust call-back test used in ocean pixels is expanded to the ocean and land pixels together with the constraint of spatial homogeneity test (Step 8 in Table 1).

After the masking in the 0.5×0.5 km^2 resolution level, the remaining pixels are aggregated to Level 2 product resolution of 6×6 km^2. Spectral TOA reflectance of remaining pixels is averaged if the number of remaining pixels is greater than 72 (Step 9 in Table 1). In this step, the discarding of the darkest 20% and brightest 40% of pixels for cloud shadow, remaining cloud, or surface contamination is implemented according to Choi et al. (2016). The quality assurance value of V1 algorithm was determined per the remaining number of pixels among 12×12 pixels after all masking procedures and also the range of retrieved AOD. The QA of 0, 1, 2, or 3 of the V1 AOD was determined according to the number of remaining pixels greater than or equal to 6, 15, 22, or 36, respectively. Also, the retrieved AOD value within the prescribed range of −0.05 and 3.6 were allocated as the QA of 1, 2, or 3, and the retrieved AOD values between −0.1 and −0.05 or between 3.6 and 5.0 were allocated as QA flag of 0. In the V2 algorithm, however, the retrieval is implemented if the number of remaining pixels is greater than 28 and the QA separation is eliminated. Also, only pixels of retrieved AOD within −0.05 and 3.6 are available and others are not retained.

After the pixel aggregation procedure, merged TOA reflectance as 6×6 km^2 resolutions are filtered out again. Bright and inhomogeneous pixels within 12×12 pixels are filtered out using the mean and *Stddev* at 412 nm (Step 10 in Table 1), and bright pixels at 412 and 660 nm together are also filtered out (Step 11 in Table 1). Furthermore, pixels of low atmospheric signal (dark at 412 nm) but high surface signal (bright at 660 nm) such as arid area are also masked out to avoid misidentification of the bright surface signal as aerosol (Step 12 in Table 1).

2.3 Climatological land surface reflectance database from multi-year samples

Surface reflectances over land and ocean are handled differently in the GOCI YAER algorithm. A minimum reflectance technique to specify the surface reflectance from the composited Rayleigh corrected reflectance (RCR) in each month and hour is applied over all land and turbid water pixels in the V1 algorithm. The GOCI YAER V1 algorithm was not capable of NRT processing because it required a monthly database encompassing the day of retrieval for the determination of surface reflectance.

For the NRT retrieval in the V2 algorithm, climatological land surface reflectances at each channel, hour, and month are calculated using a 5-year interval, which ranges from March 2011 to February 2016. The V1 surface reflectance database pixel size was 6 × 6 km^2 resolution aggregated of 12 × 12 pixels to extend the number of RCR samples. An assumption of the V1 surface reflectance was that surface reflectance within 6 × 6 km^2 is homogeneous. The V1 surface reflectance causes slightly negative AOD bias at low AOD range over Korea and Japan during 2012 spring, which means surface reflectance was overestimated (Choi et al., 2016). In the V2 algorithm, temporal RCR samples are expanded from one year to 5-year intervals, thus a possibility to find atmospheric low aerosol conditions could increase and result in darker surface reflectance compared to that of the V1 algorithm. Also, spatial resolution of climatological land surface reflectance in the V2 algorithm is 0.5 × 0.5 km^2 as original L1B TOA reflectance resolution compared to 6 × 6 km^2 resolution of the V1 algorithm. This reflects the complexity of highly spatially variable surface reflectance and allow for selection of identical pixels of TOA and surface reflectance of 0.5 × 0.5 km^2 resolution in the pixel aggregation procedure. For the determination of one pixel's surface reflectance, the maximum number of composited 5-year RCR samples is 155 (31 days × 5 years). Darkest samples (0-1% lowest in the aggregate) are assumed as cloud shadow and brighter samples (3-100%) are assumed to be affected by aerosol and/or cloud. Thus, darker 1-3% of the RCR samples are averaged and determined as surface reflectance, which are identical criteria with the V1 algorithm. The composite procedure is implemented for each month, hour, and channel samples. Each month surface reflectance climatological data represents a middle of each month (day 15) and is linearly-interpolated to retrieval date.

2.4 Climatological ocean surface wind speed database from multi-year samples

To calculate dark ocean surface reflectance, the GOCI YAER V1 algorithm uses the ECMWF wind speed at 10 m above sea level reanalysis data, which has 6-hour temporal resolution and 0.25° × 0.25° spatial resolution. The temporal ECMWF data are interpolated to those at hourly observation time. In the V2 algorithm, the wind speed reanalysis data are also replaced with climatological data from averaging 5-year data. The wind speed of 5 years at each month, hour and 0.25° × 0.25° area is averaged, which reflects seasonality such as higher in winter and lower in summer, and spatial distribution such as higher in open sea and lower in coast. Similarly as for the temporal interpolation of land surface reflectance, each month wind speed climatological data also represents a middle of each month (day 15) and is linearly-interpolated to retrieval date.

2.5 Refined pixel allocation for the land, turbid water, and dark ocean algorithms and inversion conditions

The GOCI YAER V1 land algorithm is applied not only over land pixels but also over highly turbid or high AOD ocean pixels, and ocean algorithm is applied only over dark ocean surface pixels. A pixel with $\Delta\rho_{660}$ below −0.05 is assumed as dark ocean and are processed through the dark ocean algorithm. Pixels with $\Delta\rho_{660}$ within −0.05 and −0.01 are classified as turbid water, thus go through the land algorithm. And, pixels with $\Delta\rho_{660}$ above −0.01 are regarded assumed as highly turbid water and masked out (Step 13 in Table 1). In addition, $\Delta\rho_{660}$ sometimes show above −0.05 for ocean pixels with extremely low TOA reflectance which could come from very few aerosols coupled with dark ocean surface reflectance. This misidentification results in negative AOD over the dark ocean. Therefore, the threshold test to separate extremely dark ocean pixels using TOA reflectance at 660 nm of 0.07 is added in the V2 algorithm. If a pixel show $\Delta\rho_{660}$ within −0.05 and −0.01 but TOA reflectance at 660 nm below 0.07, then dark ocean algorithm is applied.

The channels selected for the inversion from measured reflectance to aerosol optical properties are different for land, turbid water, and dark ocean pixels, respectively. In the V1 algorithm, the land and turbid water pixels use channels in which surface reflectance is less than 0.15, and the dark ocean pixels use all eight channels. In the V2 algorithm, channels used for land pixels are not changed, but the channel selection for turbid water and dark ocean pixel is different. In the atmospheric correction for the ocean color retrieval, the main assumption is that water-leaving radiance is close to zero in near-IR, thus near-IR bands are used for estimating aerosol in the atmosphere. The aerosol signal in visible is estimated from the near-IR measurements and relationship of aerosol signal between visible and near-IR according to aerosol type. Ocean color in visible is then subsequently retrieved after atmospheric correction. When aerosol optical properties are the main retrieval target, meanwhile, water-leaving radiance is handled roughly as a climatological value or neglected. Both approaches have limitations because the accurate separation of ocean color and aerosol is difficult. Because the water-leaving radiance is not considered in the current ocean surface reflectance of the GOCI YAER algorithm, channels of high water-leaving radiance are excluded in the V2 algorithm to minimize their effect (Ahn et al., 2012). Thus, only two channels of 412 and 865 nm are used over turbid water pixels with the climatological surface reflectance database, and four channels of 412, 443, 745, and 865 nm are used over dark ocean pixels with the climatological surface wind speed database.

2.5 Qualitative comparison of GOCI YAER V2 AOD with other data

For qualitative verification of whether introduced masking techniques and climatological data utilized are reasonable, a retrieved scene of GOCI YAER V2 AOD of 5 May 2015 is compared with that of V1 with all quality assured (All QA) pixels and also only for the highest quality assured (QA of 3) pixels, and additionally to that of MODIS/Aqua DT and DB, and VIIRS EDR products (Figure 2). Overpass times of MODIS and VIIRS are generally near 04 UTC over Korea peninsula, thus GOCI 04:30 UTC results are selected for comparison.

Most land pixels of Korean peninsula and Japan are not masked out and retrieved as low AOD in DT, DB, and EDR. The DB algorithm retrieves high AOD over the bright surface of Manchuria located in about 44°N and 126°E, but the DT and EDR don't retrieve AOD of those pixels because the algorithms are optimized for the dark surface reflectance. The DT, DB and EDR AOD are about 0.7-1.2 over the land pixels of Hebei in China located in about 38°N and 117°E. Meanwhile, masked pixels due to the bright sun glint ocean pixels are located in the Yellow Sea and East Sea for MODIS and VIIRS, respectively. Thus, The EDR algorithm captures an aerosol plume of AOD about 0.8 over the Northern Yellow Sea and the DT algorithm captures an aerosol plume of AOD about 0.6 over the East Sea close to Hokkaido of Japan, but not vice versa. The GOCI V1 with all QA also shows low AOD at that area, but remaining cloud contamination results in high and inhomogeneous AOD, especially at the edge of cloud. For GOCI, sun-glint masked ocean pixels are located in lower latitude than MODIS and VIIRS, thus both of these aerosol plumes detected in MODIS and VIIRS respectively are detected. Although the GOCI YAER algorithm targets the dark land surface reflectance pixels such as MODIS DT and VIIRS EDR, aerosol plume over bright land surface in Manchuria captured in DB is also detected. But it is hard to determine whether these pixels are from cloud contamination or bright land surface reflectance, or actual real high AOD.

When additional filtering as QA of 3 is applied in the V1 algorithm, most of high and inhomogeneous AOD pixels typically caused by remnant cloud contamination are removed well, but low AOD pixels over land in Korea and Japan are also removed. There are two possible reasons for extensive masking of V1 with QA of 3 for low AOD case over land. The V1 algorithm's spatial inhomogeneity test is a simple *Stddev* of 3 × 3 pixels TOA reflectance with one tight threshold regardless of TOA reflectance. It works successfully in high AOD cases, but does not work well in low AOD cases because inhomogeneous surface reflectance signals show high *Stddev* and therefore results in excessive masking. The other reason could be that those pixels are retrieved as negative AOD below −0.05 due to overestimation of surface reflectance.

Compared to the V1, the spatial variability tests of V2 cloud masking algorithm consist of the same simple *Stddev* test except for a relaxed threshold, and the additional mean-weighted *Stddev* test and the ratio test of brightest and darkest pixels, which are relative to TOA reflectance. Also, darker land surface reflectance is obtained from the climatological data and this results in increased AOD pixels compared to large negative AOD in V1. Thus, the pixels of GOCI V2 are not masked out and are retrieved well as positive low AOD, and show less inhomogeneous features at the cloud edge similar with MODIS and VIIRS AOD.

3 Long-term validation of GOCI YAER V2 AOD and AE

3.1 Ground-based measurement and ancillary satellite data

Two ground-based observation network (AERONET and SONET) data are used for quantifying the accuracy of GOCI YAER V2 AOD (τ_{G-V2}) from March 2011 to February 2016. The Aerosol Robotic Network (AERONET) of CIMEL sun-sky radiometer photometer is a ground-based aerosol remote sensing network maintained by the Goddard Space Flight Center, National Aeronautics and Space Administration (Holben et al., 1998). Spectral AOD and AE are retrieved from the direct solar irradiance measurement, and other optical/microphysical properties such as volume size distribution and refractive indices are retrieved from inversion of spectral AOD plus diffuse sky radiance measurements. Uncertainties of AERONET AOD (τ_{A}) in the visible and NIR were reported as ±0.01 (Eck et al., 1999) which is much higher accuracy than satellite-retrieved AOD because of essentially no influence from surface reflectance and in the direct solar irradiance measurement, plus highly accurate calibration. Thus, AERONET AOD is used as the reference dataset for satellite AOD validation. The fully calibrated and cloud screened AERONET Version 2 Level 2.0 AOD at 550 nm are used in this study (Smirnov et al., 2000). A total of 27 AERONET sites within GOCI observation domain, excluding specific short-period campaign sites, are selected for this analysis. The Sun-Sky Radiometer Observation Network (SONET) of CIMEL sun-sky radiometers is also a ground-based aerosol remote sensing network maintained by the Institute of Remote Sensing and Digital Earth, Chinese Academy of Sciences (Li et al., 2015). The SONET also provides spectral AOD (τ_{SONET}) from direct sun measurements and AE. A total of 6 SONET sites in China are selected for the validation of AOD at 550 nm (http://www.sonet.ac.cn).

Also, the GOCI V1 AODs with all QA ($\tau_{G-V1allQA}$) and only QA of 3 ($\tau_{G-V1QA3}$) are compared to V2 to quantify the improvement from the V1 to the V2 algorithm. The MODIS DT AOD (τ_{MDT}) and DB AODs (τ_{MDB}) of the best quality (QA of 3) are also compared over the same site and during the same period to verify the GOCI AOD accuracy relative to them. Note that the VIIRS EDR AOD is used in qualitative comparison in the previous section, but not included in the validation because the VIIRS data are only available starting from January 2013.

3.2 Collocation criteria between ground- / satellite-based measurements

The comparison between satellite and ground-based data is implemented with spatial and temporal collocation criteria. Hourly GOCI AOD pixels which are located within 25 km radius circle centered at the ground site are averaged and ground-based observation data within 30 minutes centered at every GOCI observation time are averaged. The averages of both datasets respectively are done if at least one datum of each measurement is available. The collocation criteria of MODIS data are also the same as GOCI. After the collocation, 27 AERONET sites and 6 SONET sites are matched with GOCI land AOD and 17 AERONET sites are matched with GOCI ocean AOD. Note that the 27 AERONET sites matched with GOCI land AOD includes all of the 17 coastal AERONET sites matched with GOCI ocean AOD.

3.3 Statistical evaluation metrics

Based on Sayer et al. (2014), the statistical metrics for the evaluation contain the number of collocation data (*N*); the Pearson's linear correlation coefficient (*R*); the median bias (*MB*); the root mean square error (*RMSE*); and *f*, the fraction within the expected error range of the MODIS DT AOD (Collection 5), $\mathrm{EE_{MDT}} = \pm(0.05 + 0.15 \times \tau_{A})$, referred in Levy et al. (2007). Each AOD product has respective expected error range which can be changed depending on algorithm performance. Thus, EE_{MDT} is applied to whole algorithms to compare accuracies. Note that the expected error range of GOCI YAER V2 AOD (EE_{G_V2}) will be estimated independently in the next section.

3.4 Validation of GOCI YAER V2 land AOD and comparison with other data

The comparison results of between AERONET/SONET AOD and GOCI retrieved AOD over land and ocean are presented in Figure 3, and statistics are summarized in Table 2. As shown in the qualitative comparison results (in Figure 2), $\tau_{G\_V1allQA}$ shows many overestimated points compared to τ_A due to remaining cloud contamination. About 20 % of pixels are filtered out with QA of 3 criteria (τ_{G_V1QA3}), and it results in the reduction of the number of overestimated points, decreased *RMSE* from 0.24 to 0.18, and increased *R* from 0.86 to 0.92. However, underestimated points due to the overestimation of surface reflectance remain which results in an increase negative median bias from −0.01509 to −0.06581. The comparison results of τ_{G_V2} with τ_A shows less overestimated points compared to those of $\tau_{G\_V1allQA}$ due to the improved pixel masking procedure. It results in increased the number of collocated points, *f* within EE_{MDT} and decreased *MB* and *RMSE* compared to the counterpart of τ_{G_V1QA3}. The increased number of *N* comes from the low AOD points that are filtered out in τ_{G_V1QA3}. The number of underestimated points in the low AOD range decreased due to the decreased surface reflectance using 5-year samples. It results in less bias (*MB* of 0.01947), decreased *RMSE* (0.16) and increased *f* within EE_{MDT} (0.60). The *R* of 0.91 is similar with the counterpart of τ_{G_V1QA3} (0.92). The *N* between τ_A and τ_{G_V2} is about 14 times greater than the τ_{MDT} and τ_{MDB} counterpart, mostly due to hourly data from GOCI versus twice only daily overpasses from MODIS. The comparison points of MODIS and AERONET are less spread from the one-to-one line, and it results in higher *f* within EE_{MDT} (0.62 in τ_{MDT} and 0.73 in τ_{MDB}). The *R* and *RMSE* of τ_{MDT} and τ_{MDB} are similar with the τ_{G_V2}. The *MB* of τ_{MDB} is closest to zero (0.007057), and τ_{MDT} shows positive *MB* of 0.042744. The overestimation of τ_{MDT} is reported as due to the urbanization effect of biased reflectance estimation (Munchak et al., 2013) and corrected in the MODIS DT research algorithm (not shown here) through the modified urban surface reflectance algorithm (Gupta et al., 2016).

In the comparison between SONET AOD and satellite retrieved AOD over land, the τ_{G_V2} shows better accuracy than τ_{G_V1QA3} except for the *R*. The reason of decreased *R* of τ_{G_V2} could be the utilization of an identical climatology surface reflectance for each year although in reality surface reflectance changes annually. The τ_{MDB} shows least *MB*, *RMSE*, and highest *f* within EE_{MDT}. The τ_{MDT} shows positive *MB* of 0.104176.

In conclusion, most statistical parameters show that land τ_{G_V2} accuracy is better than τ_{G_V1QA3} and comparable with τ_{MDT} and τ_{MDB}.

3.5 Validation of GOCI YAER V2 ocean AOD and comparison with other data

The changes of GOCI YAER algorithm over ocean from the V1 to V2 are the cloud masking techniques, the utilization of climatological wind speed data instead of an immediate dataset of each date, the alteration of pixel classification thresholds, the criteria between turbid water and dark ocean algorithm selection, and the selected spectral channels applied. The validation results of τ_{G_V1QA3} compared to $\tau_{G\_V1allQA}$ shows decreased *N* and *RMSE*, *MB* closer to zero, and increased *R* and *f* within EE_{MDT}, which is similar to the results over land sites except for *MB*. The refinement of the ocean algorithm from the V1 to V2 results in all improved statistics, which are increased *R* from 0.88 to 0.89, decreased *MB* from 0.042779 to 0.008028, increased f within EE_{MDT} from 0.62 to 0.71, and decreased *RMSE* from 0.13 to 0.11. The *MB* closer to zero means that the changed selection of channels in turbid water and dark ocean algorithms to avoid the effect of water-leaving radiance variation works effectively. The *N* between τ_A and τ_{G_V2} over ocean is about 27 times greater than the τ_{MDT} counterpart, which is greater than that of land comparison despite of the same difference in observation frequency. The reason is that most turbid water pixels near coast are filtered out in the MODIS DT algorithm while those are retrieved in the GOCI YAER algorithm. Compared to the ocean τ_{MDT}, the ocean τ_{G_V2} shows slightly higher *RMSE*, *MB* closer to zero, slightly higher correlation coefficient, and slightly lower *f* within EE_{MDT}. In conclusion, most statistical parameters show that ocean τ_{G_V2} accuracy is also better than τ_{G_V1QA3} and comparable with τ_{MDT}.

3.6 Comparison of AOD histogram distribution

In Figure 4, a mean of relative frequency histograms of land τ_A, collocated with GOCI and MODIS land AODs, shows a mode near 0.11 (0.10-0.12), which is the value that appears most frequent in the histogram and right-skewed distribution, and it is similar to the global τ_{MDT}, and τ_{MDB} mode of 0.1 in Sayer et al. (2013). The mode of land τ_{G_V1QA3} is about 0.03 (0.02-0.04) and those of τ_{G_V2}, τ_{MDT}, and τ_{MDB} are all 0.13 (0.12-0.14) similar to that of τ_A. Improvement of the land surface reflectance in V2 resulted in reduced mode difference between AERONET and GOCI. The histogram shape of τ_{MDB} is better matched with that of τ_A in the AOD range between 0.05 and 0.3 compared to the τ_{MDT} and τ_{G_V2}. The land-targeted histograms of τ_{MDT} and τ_{G_V2} show similar shape each other. The two histograms show lower frequency at the mode and higher frequency than that of τ_A where AOD is between 0.3 and 0.7. These results are coincident with higher positive MB of τ_{G_V2} and τ_{MDT} compared to τ_{MDB}. The τ_{G_V2} shows smoother shape due to larger number of coincident data points.

The mean of relative frequency histograms of τ_A, collocated with GOCI and MODIS ocean AODs, shows a mode near 0.11 (0.10-0.12), and those of ocean τ_{G_V1QA3} and τ_{MDT} show a mode near 0.15 (0.14-0.16). However, the ocean τ_{G_V2} shows a mode near 0.09 (0.08-0.10), which is closer than that of τ_{G_V1QA3} and τ_{MDT}. Although the mode of ocean τ_{MDT} is higher than that of τ_A, the magnitude of the peak is similar. The histogram distributions of ocean τ_{G_V1QA3} and τ_{G_V2} show lower magnitude of peak and more gradual decreases as AOD increases compared to the τ_A counterpart.

3.7 Fitting residuals change in inversion procedure

The fitting residuals (FR) of retrieved AOD is defined as the standard deviation of 550 nm AODs retrieved independently from different measured satellite spectral channels. The FR is sensitive to retrieved AOD because the standard deviation can be higher for higher AOD. Thus, the normalized FR is more suitable for comparison between V1 and V2 performance. The

FR can be calculated per each successfully retrieved pixels and the AOD accuracy could be better as the normalized fitting residuals are smaller. Thus, the histogram of normalized FR over land and ocean are analyzed using the data from 1 March 2012 to 28 February 2013 (1 year), 02-04 UTC (Figure 5).

First the ocean AOD shows decreased normalized FR in V2 (mean of 0.057) compared to V1 (mean of 0.065). The surface reflectance assumption of V1 and V2 ocean algorithms is identical and only the selected channels for AOD inversion is different. Compared to the whole eight channels utilization in V1 ocean algorithm, only four channels (412, 443, 745, and 865 nm) are used in V2 ocean algorithm to reduce the effect of ocean bio-optical variability. Because the assumption of surface reflectance is not changed, it is verified that the change of channels results in reduced FR here and the reduced mean bias. The normalized FR of land AOD also decreased from V1 (0.056) to V2 (0.052), but the difference is not big as ocean. Compared to the change of channels in ocean with identical surface reflectance assumption in ocean, the main difference over land is the change of surface reflectance. Also, the improvement of cloud masking in V2 could result in reduced normalized FR in both the ocean and land AOD.

3.8 Validation of GOCI YAER V2 AE over ocean and land

The AE inter-comparisons between AERONET and GOCI YAER V2 over ocean and land are presented in Figure 6. It is only for AERONET AOD > 0.3 because AE has large error due to the surface reflectance error when AOD is low. Note that GOCI AE is derived from the combination of selected aerosol model's pre-defined values, not from the retrieved spectral AODs. Compared to the AE of V1 products accuracy during the DRAGON-NE Asia 2012 campaign described in Choi et al. (2016) (R = 0.678 over land and ocean together), the land and ocean AE of V2 products shows lower linear correlation with AERONET (R = 0.505 and 0.459, respectively) from the 5-year validation. The DRAGON-NE Asia 2012 campaign was in spring (March-April-May) when long-range transport of Yellow Dust from the Gobi and Taklamakan Desert of the continent of Asia, which has low AE with high AOD, are more frequent. The aerosol plumes with low AE and high AOD can be retrieved with higher accuracy compared to the general low AOD cases in other seasons. Thus, AE could show higher linear correlation in spring (R of 0.63 over land and 0.57 over ocean), but lower for other seasons results (R of 0.24 over land and 0.22 over ocean). The highest frequency of points is close to the one-to-one line, but there is significant discrepancy where AERONET AE is about 1.3 but GOCI AE is about 0.6, especially over land. It could be from the different surface reflectance errors for each channel or perhaps due to a local minimum problem induced from the LUT approach for inverse modeling.

4 Error analysis of GOCI YAER V2 AOD

The retrieved AOD likely have both a bias and random error according to various factors such as sun-earth-satellite geometry, cloud contamination, surface type, assumed aerosol model, and etc. Thus, an error analysis of satellite AOD can help to understand characteristics of these products. In this section, coincident GOCI and AERONET AOD are analyzed to quantify bias and random error. The bias analysis is implemented for the four GOCI products, which are V1 land AOD with QA of 3, V2 land AOD, V1 ocean AOD with QA of 3, and V2 ocean AOD. Also, the pixel-level uncertainty of the GOCI version 2 land and ocean AODs are estimated.

4.1 Bias analysis

4.1.1 Bias as a function of AERONET AOD

In Figure 7a, the V1 land AOD has negative bias in the low AOD range due to the overestimation of surface reflectance. After implementing the climatological surface reflectance over land, the V2 land AOD shows less bias compared to the that of V1 and are distributed near 0 in the whole AOD range. This results from the increased probability of finding observation days with less aerosol loading when using a 5-year data interval. The V2 ocean AOD shows a positive bias about 0.05-0.1 and high positive bias of 0.1 near to the AERONET AOD of 0.3. The reason for the positive bias of ocean AOD could be an insufficient assumption of ocean surface reflectance considering only climatological averaged wind speed and geometry in spite of changeable surface properties including bio-optical properties. Details of improvements to the ocean AOD are described later. The range of 16^{th} - 84^{th} percentiles of both of land and ocean AOD become wider as AERONET AOD increases, plus the shapes of ranges are not symmetric.

4.1.2 Bias as a function of AERONET AE

The V2 ocean and land AOD biases are higher at the lowest AE of 0.3 corresponding to large size particles such as dust (Figure 7b). Random errors of both land and ocean AOD increase at low AE. This could be due to the assumed aerosol optical properties of large particles although non-spherical properties are already considered in the algorithm. The multi-angle measurements such as Polarization and Directionality of the Earth's Reflectances (POLDER), MISR, Airborne Multi-angle Spectro Polarimetric Imager (AirMSPI) or the planned Multi-Angle Imager for Aerosols (MAIA) can observe one target pixel with several angles so that it has the strength of determining non-spherical properties of dust particles with a more accurate phase function characterization (Diner et al., 1998; Diner et al., 2013).

4.1.3 Bias as a function of scattering angle

In Figure 7c, the bias of ocean AOD changes from −0.05 to 0.1 as scattering angle increases from 110° to 175°. That of land AOD also shows similar tendency, but the range of variance is from −0.05 to 0.05. As the scattering angle increases up to 180°, the atmospheric contribution becomes lower than that from the surface in the total TOA reflectance due to the shorter light path length, which increases AOD retrieval error (Sayer et al., 2013). This larger error at higher scattering angle is more distinct in the ocean AOD than the land AOD due to the difference in the surface reflectance between them. The land algorithm employs characterization of each hour of surface reflectance with the composite method to reflect the BRDF effect, and the ocean algorithm also considers the BRDF with geometry and wind speed. However, ocean bio-optical properties such as chlorophyll (*Chl*) or color dissolved organic matter (CDOM) are not considered in the current ocean surface reflectance so this may be the reason that the error is relatively larger in the ocean AOD versus land AOD.

4.1.4 Bias as a function of NDVI

The bias analysis of land and ocean AOD according to NDVI is presented in Figure 7d. The V2 land AOD shows bias close to zero in the range of NDVI greater than 0.4 corresponding to high vegetated region, but shows positive bias up to 0.05 in the 0.1-0.4 NDVI range corresponding to less vegetated areas such as semiarid and urban regions. The method of surface reflectance determination from multi-year samples in the V2 algorithm is applied to all pixels identically regardless of surface type, which can result in different bias features according to NDVI. The positive bias over urban areas is similar to that of MODIS Collection 6 DT AOD (Munchak et al., 2013; Gupta et al., 2016). The positive bias of V1 ocean AOD is reduced in the V2 counterpart generally because the 500-600 nm channels that are highly affected by ocean bio-optical properties variance are not used in the V2 ocean algorithm. However, other selected channels can still be affected slightly, thus there remains positive bias feature in the range of smaller negative NDVI corresponding to less turbid ocean pixels where ocean surface models considering wind speed are utilized.

4.1.5 Bias as a function of cloud contamination

Despite applying several cloud masking techniques, remaining cloud contaminated pixels could still result in high positive biases in AOD. In the aggregation step of collecting 12 × 12 pixels, from 500 m pixels to 6 × 6 km^2, the maximum number of used pixels is 58 among 144 pixels by discarding the darkest 20% and brightest 40% of pixels. The minimum number of pixels required to retrieve aerosol products is set as 29, which corresponds to 50% of available number of pixels after the discarding (58). Thus, the cloud fraction (CF) within one aerosol product pixel could have the range from 0 to 0.5 according to the finally remaining number of pixels from 58 to 29. Note that the brighter pixels due to surface reflectance, not cloud, could be counted as high CF, but it is hard to distinguish them perfectly in the 500 m spatial resolution. In Figure 8a, the bias of ocean AOD is close to zero at CF of 0.0, and positively increases up to 0.1 as CF increases up to 0.5. The bias of land AOD is about 0.05 at the CF close zero, decreases close to zero in the CF range about 0.05-0.25, and increases up to 0.05 in the CF up to 0.4. The positive bias of land AOD at CF of 0 could be the influence of surface reflectance overestimation. The bias due to the cloud contamination could be also analyzed according to the number of spatially collocated GOCI AOD pixels (N_C) with each AERONET site location (Figure 8b). Because the GOCI AODs within 25 km radius centered on the site are averaged if only one pixel is available at least, N_C can be regarded as related with CF, indirectly. Note that the maximum N_C of ocean AOD pixels of 40 is less than that of land (56) because ocean AOD is generally collocated with the AERONET site located on the coast. The bias of V2 land AOD is 0.1 if N_C is only one, and it decreases close to zero as N_C becomes higher. The V1 land AOD had negative bias primarily due to the surface reflectance, thus the bias is not changed according to N_C. The ocean AOD bias is 0.05 at N_C of 1, and decreases for higher N_C up to 30. But, it shows high positive bias for N_C greater than 30, which could be due to problems in characterizing ocean surface reflectance. In addition, the parameter *Stddev* of the spatially collocated AODs indicates how spatially smooth the retrieved AOD are. In the GOCI algorithm, aerosol optical properties of each pixel are retrieved independently regardless of surrounding pixels, which is similar to the concept of the MODIS DT and DB algorithms (Levy et al., 2013; Hsu et al., 2013). The *Stddev* could increase if cloud contaminated pixels are retrieved as high AOD in spite of relative low AOD of surrounding pixels, thus it also may indicate cloud contamination indirectly in this each-pixel-retrieval concept. In Figure 8c, the bias increases positively up to about 0.13 for ocean AOD and about 0.08 for land AOD as the *Stddev* increases, and the range of 16^{th} - 84^{th} percentiles also becomes wider. The V1 land AOD had a negative bias of -0.1 for low *Stddev* and it was about −0.05 in the high *Stddev* range, which was persistently affected by the surface reflectance issues and/or cloud contamination. Note that some recent aerosol retrieval algorithms adopt the concept of statistically spatial smoothness constraint of aerosol optical properties in the inversion procedure for better accuracy (Dubovik et al., 2011; Shi et al., 2016; Xu et al., 2016).

4.1.6 Bias as a function of hour, month, and year

The GOCI AOD consists of eight, hourly observations per day from 09:30 to 16:30 KST (centered time of each measurement), and the solar zenith and azimuth angle varies over a much wider range than that from LEO satellites. It requires more sophisticated assumptions such as surface reflectance, aerosol phase function, or calculation of Rayleigh scattering, which may result in different accuracies according to measurement time. In Figure 9a, the bias of land AOD decreases from about −0.1 of V1 to almost zero of V2, and its hourly dependence of V2 is indistinct. In contrast, the ocean AOD shows a distinct diurnal shape of bias, which is close to zero at the 09:30, 15:30, and 16:30 KST and about 0.1 at 12:30 KST. This coincides with the results of bias analysis according to the scattering angle.

The bias of land AOD as a function of month is not changed and kept as almost zero (Figure 9b). In contrast, that of ocean AOD increases up to 0.1 in the spring of April-May and about 0.05 in the late fall and early winter of November and December, which is likely relevant to the monthly *Chl* concentration variation over East Asia. The climatological *Chl* concentration reported by Yamada et al. (2004) shows highest as about 1.2-2.7 μg/l in spring and about and 0.8-1.2 μg/l in late fall compared to the 0.2-0.4 μg/l in other seasons. Thus, the monthly bias change of ocean AOD probably is affected by the *Chl* concentration in the current GOCI ocean AOD algorithm. The positive biases of the V1 ocean AOD in spring and late fall became small in the V2 ocean AOD after changing channels utilization.

The V1 land AOD retrieved using each month of each year surface reflectance show constant negative bias about −0.05 from 2011 to 2015 (Figure 9c). In contrast, the V2 land AOD retrieved using monthly climatological surface reflectance data from the 5-year interval samples shows that biases are smaller than those of V1 but with increased variation compared to those of V1. The increased variance for V2 could be a limitation of the climatological data application which cannot reflect year-to-year changes of surface reflectance. The ocean AOD shows less variation of biases compared to the V2 land AOD, but not as constant as the V1 land AOD. This could possibly be attributed to inter-annually variable ocean surface reflectance according to ocean bio-optical properties.

4.2 Uncertainty estimation of GOCI YAER V2 AOD

The "uncertainty" (or "expected error") of retrieved AOD is defined as the one-standard-deviation confidence interval corresponding to 68th percentile, and is estimated from the long-term evaluation of retrieved satellite AOD using ground-based AERONET measurement. Each satellite-retrieved AOD has own uncertainty according to the algorithm characteristics such as surface reflectance estimation, assumed aerosol models, etc. The expected error (EE) of retrieved AOD can be estimated as a function of AERONET AOD and retrieved satellite AOD itself, respectively. A "diagnostic" expected error (DEE) is based on AERONET AOD, relatively more accurate than satellite AOD, so that it is useful to evaluate the algorithm quantitatively itself, but it is restricted only for AERONET pixels. Instead, the "prognostic" expected error (PEE), a function of retrieved satellite AOD, can be calculated over all retrieved pixels so that it is more appropriate for the application such as data assimilation with air quality forecasting models (Sayer et al., 2013; Shi et al., 2013). The common characteristic of EE is that EE increases linearly as AOD increases. Thus, a linear regression equation between 68th percentile of absolute error and reference AOD (AERONET or satellite AOD) are determined as EE. The 68th, 38th, and 95th percentile points should be corresponding to one, half, and two standard-deviation intervals, respectively, assuming the error has Gaussian distribution and no bias. Then, half and double of the linear least square regression equation of 68th percentile should follow the 38th and 95th percentile points. The EE of MODIS, VIIRS, and GOCI AOD based on this approach are summarized in Table 3. Note that additional consideration in EE is applied to each algorithm differently, such as bias information in MODIS DT over ocean and VIIRS EDR or geometrical air mass factor in MODIS DB (Huang et al., 2016; Sayer et al., 2013; Levy et al., 2013).

To estimate DEE and PEE of GOCI YAER V2 AOD using a linear least square regression equation, the absolute AOD difference between GOCI and AERONET is analyzed according to AERONET and GOCI AOD respectively in Figure 10. The linear DEE ($0.183\tau_A + 0.037$) and PEE ($0.206\tau_G + 0.030$) of ocean AOD follow the 68th percentile points well (R = 0.969 and 0.964, respectively). The double of DEE and PEE of ocean AOD are well-matched with the 95th percentile points. Although the linear DEE ($0.135\tau_A + 0.075$) and PEE ($0.192\tau_G + 0.060$) of land AOD are well-matched with the 68th percentile points (R = 0.969 and 0.930, respectively), the PEE of land AOD shows different discrepancies according to AOD range. The discrepancy is significant between 95th percentile points and double of PEE of land AOD. Due to the existence of more complex error sources, the EE of land AOD cannot be accurately characterized as a linear relation with AOD (Hyer et al., 2011). The estimated linear DEE and PEE of land AOD shows similar or lower slope but higher offset compared to the MODIS and VIIRS which is presumed due to higher surface reflectance bias in GOCI.

Instead, the PEE constructed differently according to specific AOD ranges ("multiple PEE") are applied as in Figure 11 and summarized in Table 4. The "noise floor", defined in Hyer et al. (2011), is the minimum absolute error so that PEE should be greater than that value. The fifth-order polynomial regression fitting is applied when GOCI AOD is less than 0.5 to reflect the curved pattern, and linear fitting is applied when GOCI AOD is greater than 0.7. The higher value between these two relations computed values are applied when GOCI AOD is between 0.5 to 0.7. Both multiple PEEs show higher EE values about GOCI AOD of 0.1 (over ocean and land) and 0.6 (over land) compared to the linear PEEs, thus they show better matching of observed features with the 68^{th} percentile points.

Further, the ratio of actual error to linear and multiple PEE follows the theoretical Gaussian distribution with mean of zero and variance of one ($\mathcal{N}(0,1)$) as shown in Figure 12, which is similar to the results obtained from MODIS DB AOD (Sayer et al., 2013). Because the PEE of ocean AOD has strong linear relation with GOCI AOD, there are less differences between linear and multiple PEE. However, the PEE of land AOD has significantly different relationships per AOD range so that the distributions of linear and multiple PEE are also different. Although the ratio between −1 and +1 of the $\mathcal{N}(0,1)$ (0.683) is closer with that of linear PEE of land AOD (0.680) than the counterpart of multiple PEE (0.666), the peak of the $\mathcal{N}(0,1)$ is closer with that of multiple PEE than linear PEE. Also, all linear and multiple PEEs of ocean and land AOD have slight positive bias compared to the $\mathcal{N}(0,1)$. It means that obtained PEEs are imperfect due to the remaining bias characteristics analyzed in the previous section. Notwithstanding, the obtained PEEs of GOCI YAER V2 AOD, especially multiple PEE for land AOD, generally represent actual errors well.

4.3 Regional performance

The obtained GOCI DEE and (multiple) PEE can be used for AOD validation over each site along with other statistical evaluation metrics presented earlier. The validation results for all sites have been analyzed individually to show the results of each site, including the fraction within DEE and (multiple) PEE. Spatial distributions of statistical evaluation metrics are presented in Figure 13 and Figure 14 for land and ocean AOD, respectively.

The average of collocated AERONET AOD is highest in China including Beijing (0.69 and 0.48 with GOCI V1 and V2, respectively) and Taihu (0.70) sites. The Korean sites show higher annual average AERONET AOD (0.33-0.50) than Japan sites (0.17-0.30). For land AOD among 27 land AERONET sites, 21 sites show improvement in V2 by the statistical evaluation metrics and 6 sites show worse accuracy in V2 than V1. And, the GOCI V2 land AOD shows less biased and higher fraction within DEE and PEE over the Korean peninsula as compared to the China and Japan sites. The sites presenting the worst accuracy in V2 land AOD show positively increased median bias. The probable reason for worse accuracy of some sites in V2 compared to V1 is likely the way the surface reflectance database is constructed. The surface reflectances of the lower accuracy sites in V2 such as Chiba_University, Kobe, Xinglong, and Osaka are bright (urban surfaces) compared to other sites, and the current identification threshold of the darkest 1-3% of observations without considering surface type results in climatologically derived values that are too dark surface for reflectances at bright (urbanized) surface sites. Tilstra et al. (2017) suggests that selecting the mode of the RCR histogram is better for characterizing the surface reflectance of bright surfaces than selecting the minimum values of the RCR. Different thresholds according to surface type may improve the accuracy of retrievals over sites that have bright surface reflectance.

For the ocean AOD, 14 sites show improvement in V2 and 3 sites show worse accuracy in V2 than V1 among 17 coastal AERONET sites. Compared to increased median bias in land AOD, ocean AOD shows decreased median bias from V1 to V2. The lower accuracy sites don't have significant difference between V1 and V2 compared to land AOD. The fractions within DEE and PEE of V1 ocean AOD of the Japan sites are higher than the Korea sites, but it becomes similar in V2. The obtained DEE of V2 ocean AOD (94%) is too high than theoretical 1-sigma fraction (68%). However, the PEE of V2 ocean AOD is 66% as similar with theoretical value. Thus, the obtained PEE can represent error of GOCI AOD better than DEE.

5 Summary and outlook

Objective of this study is the improvement of the GOCI YAER algorithm in V2 for NRT processing with better accuracy. Overall cloud masking procedures were revised to prevent false masking of low AOD over bright surfaces as cloud in the previous version by adopting recent MODIS and VIIRS cloud masking methodology and improving existing V1 methodologies. To reduce the remaining cloud or aerosol contamination in the surface reflectance database, the period of RCR samples is expanded from each year to a 5-year interval to increase the probability of finding cloudless low AOD cases so that the climatological surface reflectance database is more accurately constructed. Also, the surface wind speed data are constructed as a climatological database for the NRT retrieval without importing numerical weather forecast products. The GOCI spectral channel selection is revised according to specific surface conditions: dark ocean, turbid water, and land surface. Especially, the channels from 500 nm to 700 nm are largely affected by ocean bio-optical variation thus excluded from ocean AOD retrieval. As a result, the area of successful AOD retrieval and masking-out in the GOCI YAER V2 algorithm and its retrieved AOD values became closer to the results of MODIS and VIIRS AOD qualitatively, compared to that of GOCI YAER V1.

To confirm improvements of GOCI AOD accuracy in V2, the retrieved GOCI AOD and MODIS AOD are compared with ground-based East Asia AERONET and China SONET measurements of AOD for 5 years from 1 March 2011 to 29 February 2016. The GOCI YAER land AOD compared to AERONET AOD showed significant improvement from V1 to V2 with reduced bias from about −0.07 to 0.02 and increased f within $\mathrm{EE_{MDT}}$ from 49% to 60%. The comparison with SONET AOD also shows consistent results with reduced bias from about −0.10 to −0.01 and increased f within $\mathrm{EE_{MDT}}$ from 42% to 52%. The GOCI YAER ocean AOD also shows reduced bias from about 0.04 to 0.01 and increased f within $\mathrm{EE_{MDT}}$ from 62% to 73%. As a result, the quality of both GOCI YAER V2 ocean and land AOD are more comparable with that of MODIS DT and DB AOD products over East Asia.

Although retrieved GOCI YAER V2 AOD shows some bias features with respect to AERONET AOD and AE, scattering angle, NDVI, cloud fraction and homogeneity of retrieved AOD, observation time, month, and year, it never exceeds absolute ~0.1 for most variables. With the characteristics that error increases as AOD increases, the intrinsic expected error of GOCI YAER V2 AOD was estimated using AERONET data. The linear DEE and PEE ($0.183\tau_A + 0.037$ and $0.206\tau_G + 0.030$, respectively) for ocean AOD represent actual error well over the entire AOD range. The linear DEE of land AOD ($0.135\tau_A + 0.075$) also represents actual error well. However, actual error doesn't increase linearly per GOCI land AOD, thus the linear PEE of land AOD ($0.192\tau_G + 0.060$) shows some differences for specific AOD ranges. Instead, multiple PEE which consists of different relationships according to specific GOCI AOD ranges represents the actual error better.

Despite the algorithm improvements shown in this study, there is still potential for future improvement. The current version of the LUT was calculated by using a scalar radiative transfer calculation which is less accurate for calculating Rayleigh scattering for the short visible wavelengths (~400 nm) and by using a plane-parallel atmosphere approximation which is less accurate in high solar/sensor zenith angle. A vector RTM calculation (i.e. consideration of polarization) and spherical-shell atmosphere approximation can calculate Rayleigh scattering in high accuracy which can improve the accuracy of the GOCI YAER algorithm. Also, recent statistically optimized aerosol retrieval algorithms utilizing characteristics of spatial and temporal smoothness constraints for aerosol show higher accuracy by increasing aerosol signal (Dubovik et al., 2011; Xu et al., 2016). They also enable of simultaneous retrieval of multi geophysical variables such as aerosol and surface reflectance over land and aerosol and chlorophyll concentration over ocean, which can reduce the remaining error due to the pre-defined surface reflectance over ocean and land in the GOCI YAER algorithm.

Hourly AOD products based on the improved GOCI YAER AOD could contribute to better understandings of aerosols in terms of long-term climate changes and short-term air quality monitoring and forecasting perspectives over East Asia, especially rapid diurnal variation and transboundary transport. Also, the second generation of GOCI to be launched in 2019, which has higher spatial resolution (~250 m), more channels including 380 nm, and full-disk coverage per day can improve the accuracy of AOPs retrieval. Furthermore, GOCI-II will observe East Asia simultaneously with the Geostationary Environmental Monitoring Spectrometer (GEMS) for trace gases (i.e. ozone, nitrogen dioxide, formaldehyde, and sulfur dioxide) and AMI for meteorological parameters (i.e. cloud properties). Therefore, multi-sensor synergies for comprehensive understandings of aerosols with trace gases, cloud, and ocean colors together are expected.

Acknowledgements

We thank the Korean Institute of Ocean Science and Technology (KIOST) for the development and application of GOCI in this research. We also thank all principal investigators and their staff for establishing and maintaining the AERONET and SONET sites used in this investigation. We also thank the MODIS and VIIRS science team for providing valuable data for this research.

References

Ahn, J. H., Park, Y. J., Ryu, J. H., Lee, B., and Oh, I. S.: Development of Atmospheric Correction Algorithm for Geostationary Ocean Color Imager (GOCI), Ocean Sci J, 47, 247-259, 2012.

Choi, J. K., Park, Y. J., Ahn, J. H., Lim, H. S., Eom, J., and Ryu, J. H.: GOCI, the world's first geostationary ocean color observation satellite, for the monitoring of temporal variability in coastal water turbidity, J Geophys Res-Oceans, 117, 2012.

Choi, M., Kim, J., Lee, J., Kim, M., Park, Y. J., Jeong, U., Kim, W., Hong, H., Holben, B., Eck, T. F., Song, C. H., Lim, J. H., and Song, C. K.: GOCI Yonsei Aerosol Retrieval (YAER) algorithm and validation during the DRAGON-NE Asia 2012 campaign, Atmos. Meas. Tech., 9, 1377-1398, 2016.

Cox, C. and Munk, W.: Statistics of the sea surface derived from sun glitter, Journal of Marine Research, 13, 198-227, 1954.

Diner, D. J., Beckert, J. C., Reilly, T. H., Bruegge, C. J., Conel, J. E., Kahn, R. A., Martonchik, J. V., Ackerman, T. P., Davies, R., Gerstl, S. A. W., Gordon, H. R., Muller, J. P., Myneni, R. B., Sellers, P. J., Pinty, B., and Verstraete, M. M.: Multi-angle Imaging SpectroRadiometer (MISR) - Instrument description and experiment overview, Ieee T Geosci Remote, 36, 1072-1087, 1998.

Diner, D. J., Xu, F., Garay, M. J., Martonchik, J. V., Rheingans, B. E., Geier, S., Davis, A., Hancock, B. R., Jovanovic, V. M., Bull, M. A., Capraro, K., Chipman, R. A., and McClain, S. C.: The Airborne Multiangle SpectroPolarimetric Imager (AirMSPI): a new tool for aerosol and cloud remote sensing, Atmos Meas Tech, 6, 2007-2025, 2013.

Dubovik, O. and King, M. D.: A flexible inversion algorithm for retrieval of aerosol optical properties from Sun and sky radiance measurements, J Geophys Res-Atmos, 105, 20673-20696, 2000.

Dubovik, O., Herman, M., Holdak, A., Lapyonok, T., Tanre, D., Deuze, J. L., Ducos, F., Sinyuk, A., and Lopatin, A.: Statistically optimized inversion algorithm for enhanced retrieval of aerosol properties from spectral multi-angle polarimetric satellite observations, Atmos Meas Tech, 4, 975-1018, 2011.

Eck, T. F., Holben, B. N., Reid, J. S., Dubovik, O., Smirnov, A., O'Neill, N. T., Slutsker, I., and Kinne, S.: Wavelength dependence of the optical depth of biomass burning, urban, and desert dust aerosols, J Geophys Res-Atmos, 104, 31333-31349, 1999.

Gupta, P., Levy, R. C., Mattoo, S., Remer, L. A., and Munchak, L. A.: A surface reflectance scheme for retrieving aerosol optical depth over urban surfaces in MODIS Dark Target retrieval algorithm, Atmos Meas Tech, 9, 3293-3308, 2016.

Harrison, R. M. and Yin, J.: Particulate matter in the atmosphere: which particle properties are important for its effects on health?, Science of The Total Environment, 249, 85-101, 2000.

Herman, J. R. and Celarier, E. A.: Earth surface reflectivity climatology at 340-380 nm from TOMS data, J Geophys Res-Atmos, 102, 28003-28011, 1997.

Holben, B. N., Eck, T. F., Slutsker, I., Tanre, D., Buis, J. P., Setzer, A., Vermote, E., Reagan, J. A., Kaufman, Y. J., Nakajima, T., Lavenu, F., Jankowiak, I., and Smirnov, A.: AERONET - A federated instrument network and data archive for aerosol characterization, Remote Sens Environ, 66, 1-16, 1998.

Hsu, N. C., Tsay, S. C., King, M. D., and Herman, J. R.: Aerosol properties over bright-reflecting source regions, Ieee T Geosci Remote, 42, 557-569, 2004.

Hsu, N. C., Gautam, R., Sayer, A. M., Bettenhausen, C., Li, C., Jeong, M. J., Tsay, S. C., and Holben, B. N.: Global and regional trends of aerosol optical depth over land and ocean using SeaWiFS measurements from 1997 to 2010, Atmos Chem Phys, 12, 8037-8053, 2012.

Hsu, N. C., Jeong, M. J., Bettenhausen, C., Sayer, A. M., Hansell, R., Seftor, C. S., Huang, J., and Tsay, S. C.: Enhanced Deep Blue aerosol retrieval algorithm: The second generation, J Geophys Res-Atmos, 118, 9296-9315, 2013.

Huang, J. F., Kondragunta, S., Laszlo, I., Liu, H. Q., Remer, L. A., Zhang, H., Superczynski, S., Ciren, P., Holben, B. N., and Petrenko, M.: Validation and expected error estimation of Suomi-NPP VIIRS aerosol optical thickness and Angstrom exponent with AERONET, J Geophys Res-Atmos, 121, 7139-7160, 2016.

Hyer, E. J., Reid, J. S., and Zhang, J.: An over-land aerosol optical depth data set for data assimilation by filtering, correction, and aggregation of MODIS Collection 5 optical depth retrievals, Atmos Meas Tech, 4, 379-408, 2011.

IPCC: Climate Change 2013: The Physical Science Basis. Contribution of Working Group I to the Fifth Assessment Report of the Intergovernmental Panel on Climate Change, Cambridge University Press, Cambridge, United Kingdom and New York, NY, USA, 2013.

Jeon, W., Choi, Y., Percell, P., Souri, A. H., Song, C. K., Kim, S. T., and Kim, J.: Computationally efficient air quality forecasting tool: implementation of STOPS v1.5 model into CMAQ v5.0.2 for a prediction of Asian dust, Geosci Model Dev, 9, 3671-3684, 2016.

Kaufman, Y. J., Tanre, D., Remer, L. A., Vermote, E. F., Chu, A., and Holben, B. N.: Operational remote sensing of tropospheric aerosol over land from EOS moderate resolution imaging spectroradiometer, J Geophys Res-Atmos, 102, 17051-17067, 1997.

Kim, J., Lee, J., Lee, H. C., Higurashi, A., Takemura, T., and Song, C. H.: Consistency of the aerosol type classification from satellite remote sensing during the Atmospheric Brown Cloud-East Asia Regional Experiment campaign, J Geophys Res-Atmos, 112, D22S33, doi:10.1029/2006JD008201, 2007.

Koelemeijer, R. B. A., de Haan, J. F., and Stammes, P.: A database of spectral surface reflectivity in the range 335-772 nm derived from 5.5 years of GOME observations, J Geophys Res-Atmos, 108, 4070, doi:4010.1029/2002jd002429, 2003.

Kopp, T. J., Thomas, W., Heidinger, A. K., Botambekov, D., Frey, R. A., Hutchison, K. D., Iisager, B. D., Brueske, K., and Reed, B.: The VIIRS Cloud Mask: Progress in the first year of S-NPP toward a common cloud detection scheme, Journal of Geophysical Research: Atmospheres, 119, 2441-2456, 2014.

Lee, E., Županski, M., Županski, D., and Park, S. K.: Impact of the OMI aerosol optical depth on analysis increments through coupled meteorology–aerosol data assimilation for an Asian dust storm, Remote Sens Environ, 193, 38-53, 2017.

Lee, J., Kim, J., Song, C. H., Ryu, J. H., Ahn, Y. H., and Song, C. K.: Algorithm for retrieval of aerosol optical properties over the ocean from the Geostationary Ocean Color Imager, Remote Sens Environ, 114, 1077-1088, 2010.

Lee, S., Song, C. H., Park, R. S., Park, M. E., Han, K. M., Kim, J., Choi, M., Ghim, Y. S., and Woo, J. H.: GIST-PM-Asia v1: development of a numerical system to improve particulate matter forecasts in South Korea using geostationary satellite-retrieved aerosol optical data over Northeast Asia, Geosci Model Dev, 9, 17-39, 2016.

Levy, R. C., Remer, L. A., Mattoo, S., Vermote, E. F., and Kaufman, Y. J.: Second-generation operational algorithm: Retrieval of aerosol properties over land from inversion of Moderate Resolution Imaging Spectroradiometer spectral reflectance, J Geophys Res-Atmos, 112, D13211, doi:13210.11029/12006jd007811, 2007.

Levy, R. C., Remer, L. A., Kleidman, R. G., Mattoo, S., Ichoku, C., Kahn, R., and Eck, T. F.: Global evaluation of the Collection 5 MODIS dark-target aerosol products over land, Atmos Chem Phys, 10, 10399-10420, 2010.

Levy, R. C., Mattoo, S., Munchak, L. A., Remer, L. A., Sayer, A. M., Patadia, F., and Hsu, N. C.: The Collection 6 MODIS aerosol products over land and ocean, Atmos Meas Tech, 6, 2989-3034, 2013.

Li, R. R., Kaufman, Y. J., Gao, B. C., and Davis, C. O.: Remote sensing of suspended sediments and shallow coastal waters, Ieee T Geosci Remote, 41, 559-566, 2003.

Li, Z., Li, D., Li, K., Xu, H., Chen, X., Chen, C., Xie, Y., Li, L., Li, L., Li, W., Lv, Y., Qie, L., Zhang, Y., and Gu, X.: Sun-sky radiometer observation network with the extension of multi-wavelength polarization measurements, Journal of Remote Sensing, 19, 495-519, 2015.

Lim, S. S. and Vos, T. and Flaxman, A. D. and Danaei, G. and Shibuya, K. and Adair-Rohani, H. and Amann, M. and Anderson, H. R. and Andrews, K. G. and Aryee, M. and Atkinson, C. and Bacchus, L. J. and Bahalim, A. N. and Balakrishnan, K. and Balmes, J. and Barker-Collo, S. and Baxter, A. and Bell, M. L. and Blore, J. D. and Blyth, F., et al.: A comparative risk assessment of burden of disease and injury attributable to 67 risk factors and risk factor clusters in 21 regions, 1990-2010: a systematic analysis for the Global Burden of Disease Study 2010, Lancet, 380, 2224-2260, 2012.

Mayer, B. and Kylling, A.: Technical note: The libRadtran software package for radiative transfer calculations - description and examples of use, Atmos Chem Phys, 5, 1855-1877, 2005.

Munchak, L. A., Levy, R. C., Mattoo, S., Remer, L. A., Holben, B. N., Schafer, J. S., Hostetler, C. A., and Ferrare, R. A.: MODIS 3 km aerosol product: applications over land in an urban/suburban region, Atmos Meas Tech, 6, 1747-1759, 2013.

Park, M. E., Song, C. H., Park, R. S., Lee, J., Kim, J., Lee, S., Woo, J. H., Carmichael, G. R., Eck, T. F., Holben, B. N., Lee, S. S., Song, C. K., and Hong, Y. D.: New approach to monitor transboundary particulate pollution over Northeast Asia, Atmos Chem Phys, 14, 659-674, 2014.

Pinty, B. and Verstraete, M. M.: GEMI: a non-linear index to monitor global vegetation from satellites, Vegetatio, 101, 15-20, 1992.

Remer, L. A., Kaufman, Y. J., Tanré, D., Mattoo, S., Chu, D. A., Martins, J. V., Li, R. R., Ichoku, C., Levy, R. C., Kleidman, R. G., Eck, T. F., Vermote, E., and Holben, B. N.: The MODIS Aerosol Algorithm, Products, and Validation, J Atmos Sci, 62, 947-973, 2005.

Saide, P. E., Kim, J., Song, C. H., Choi, M., Cheng, Y. F., and Carmichael, G. R.: Assimilation of next generation geostationary aerosol optical depth retrievals to improve air quality simulations, Geophys Res Lett, 41, 9188-9196, 2014.

Sayer, A. M., Hsu, N. C., Bettenhausen, C., and Jeong, M. J.: Validation and uncertainty estimates for MODIS Collection 6 "Deep Blue" aerosol data, J Geophys Res-Atmos, 118, 7864-7872, 2013.

Sayer, A. M., Munchak, L. A., Hsu, N. C., Levy, R. C., Bettenhausen, C., and Jeong, M. J.: MODIS Collection 6 aerosol products: Comparison between Aqua's e-Deep Blue, Dark Target, and "merged" data sets, and usage recommendations, J Geophys Res-Atmos, 119, 13965-13989, 2014.

Shi, C., Nakajima, T., and Hashimoto, M.: Simultaneous retrieval of aerosol optical thickness and chlorophyll concentration from multiwavelength measurement over East China Sea, J Geophys Res-Atmos, 121, 14084-14101, 2016.

Shi, Y., Zhang, J., Reid, J. S., Hyer, E. J., and Hsu, N. C.: Critical evaluation of the MODIS Deep Blue aerosol optical depth product for data assimilation over North Africa, Atmos Meas Tech, 6, 949-969, 2013.

Smirnov, A., Holben, B. N., Eck, T. F., Dubovik, O., and Slutsker, I.: Cloud-screening and quality control algorithms for the AERONET database, Remote Sens Environ, 73, 337-349, 2000.

Takemura, T., Nakajima, T., Dubovik, O., Holben, B. N., and Kinne, S.: Single-scattering albedo and radiative forcing of various aerosol species with a global three-dimensional model, J Climate, 15, 333-352, 2002.

Tilstra, L. G., Tuinder, O. N. E., Wang, P., and Stammes, P.: Surface reflectivity climatologies from UV to NIR determined from Earth observations by GOME-2 and SCIAMACHY, J Geophys Res-Atmos, 122, 4084-4111, 2017.

van Donkelaar, A., Martin, R. V., Brauer, M., Kahn, R., Levy, R., Verduzco, C., and Villeneuve, P. J.: Global Estimates of Ambient Fine Particulate Matter Concentrations from Satellite-Based Aerosol Optical Depth: Development and Application, Environmental Health Perspectives, 118, 847-855, 2010.

Wang, Y., Chen, L., and Shang, H.: A new cloud mask algorithm used in aerosol retrieval over land for Suo-NPP VIIRS, 356-359, 10.1109/IGARSS.2016.7729086.

WHO: Ambient air pollution: A global assessment of exposure and burden of disease. In: Ambient air pollution: a global assessment of exposure and burden of disease, 2016.

Xiao, Q., Zhang, H., Choi, M., Li, S., Kondragunta, S., Kim, J., Holben, B., Levy, R. C., and Liu, Y.: Evaluation of VIIRS, GOCI, and MODIS Collection 6AOD retrievals against ground sunphotometer observations over East Asia, Atmos Chem Phys, 16, 1255-1269, 2016.

Xu, F., Dubovik, O., Zhai, P. W., Diner, D. J., Kalashnikova, O. V., Seidel, F. C., Litvinov, P., Bovchaliuk, A., Garay, M. J., van Harten, G., and Davis, A. B.: Joint retrieval of aerosol and water-leaving radiance from multispectral, multiangular and polarimetric measurements over ocean, Atmos Meas Tech, 9, 2877-2907, 2016.

Xu, J. W., Martin, R. V., van Donkelaar, A., Kim, J., Choi, M., Zhang, Q., Geng, G., Liu, Y., Ma, Z., Huang, L., Wang, Y., Chen, H., Che, H., Lin, P., and Lin, N.: Estimating ground-level PM2.5 in eastern China using aerosol optical depth determined from the GOCI satellite instrument, Atmos Chem Phys, 15, 13133-13144, 2015.

Yamada, K., Ishizaka, J., Yoo, S., Kim, H. C., and Chiba, S.: Seasonal and interannual variability of sea surface chlorophyll a concentration in the Japan/East Sea (JES), Prog Oceanogr, 61, 193-211, 2004.

Yoon, J., Burrows, J. P., Vountas, M., von Hoyningen-Huene, W., Chang, D. Y., Richter, A., and Hilboll, A.: Changes in atmospheric aerosol loading retrieved from space-based measurements during the past decade, Atmos Chem Phys, 14, 6881-6902, 2014.

Zhang, J. and Reid, J. S.: A decadal regional and global trend analysis of the aerosol optical depth using a data-assimilation grade over-water MODIS and Level 2 MISR aerosol products, Atmos Chem Phys, 10, 10949-10963, 2010.

Atmos. Meas. Tech. Discuss., https://doi.org/10.5194/amt-2017-251
Manuscript under review for journal Atmos. Meas. Tech.
Discussion started: 7 August 2017

Tables

Table 1 Cloud and other pixel masking steps of the GOCI YAER V2 algorithm.

Sequence of steps	Conditions	Classifications	References
Masking in 0.5 × 0.5 km^2 resolution			
1	*Stddev* of TOA reflectance at 555 nm in 3 × 3 pixels > 0.0025	Cloud over ocean (whole 9 pixels)	Remer et al. (2005) Choi et al. (2016)
2	A ratio of maximum and minimum TOA reflectance at 412 nm in 3 × 3 pixels > 1.1	Cloud over land (whole 9 pixels)	Hsu et al. (2013)
3	*Stddev* of TOA reflectance at 490 nm in 3 × 3 pixels > 0.015	Cloud over land (whole 9 pixels)	Wang et al. (2016)
4	Mean-weighted *Stddev* of TOA reflectance at 490 nm in 3 × 3 pixels > 0.0025	Cloud over land (whole 9 pixels)	Wang et al. (2016)
5	TOA reflectance at 490 nm > 0.4	Cloud over ocean and land	Remer et al. (2005) Choi et al. (2016)
6	Pseudo GEMI index < 1.87	Cloud over land	Pinty and Verstraete (1992) Kopp et al. (2014)
7	NDVI using TOA reflectance at 660 and 865 nm < −0.01	Inland water over land	Hsu et al. (2013)
8	Ratio of TOA reflectance at 490 to 660 nm < 0.75, and *Stddev* of TOA reflectance at 490 nm < 0.015 (or mean-weighted *Stddev* of TOA reflectance at 490 nm < 0.0025)	Homogenous dust call-back over land and ocean	Remer et al. (2005)
Aggregation to 6 × 6 km^2 resolution			
9	The number of available pixels after masking among 12 × 12 pixels > 72	Discarding darkest 20 % and bright 40 % pixels (reference: TOA reflectance at 490 nm), and average of remaining pixels	Remer et al. (2005) Levy et al. (2007) Choi et al. (2016)
Additional masking in 6 × 6 km^2 resolution			
10	*Stddev* of TOA reflectance at 412 nm > 0.003 and mean TOA reflectance at 412 nm in 12 by 12 pixels > 0.22	Cloud over land and ocean	
11	Mean TOA reflectance in 412 nm > 0.33 and mean TOA reflectance in 555 nm > 0.33	Cloud over land and ocean	
12	Mean TOA reflectance in 412 nm < 0.30 and mean TOA reflectance in 660 nm > 0.2	Low aerosol signals and arid area masking	
13	Difference of TOA reflectance at 660 nm between direct one and linear-interpolated one from 412 and 865 nm < −0.01	Highly turbid pixels masking over ocean	Li et al. (2003) Choi et al. (2016)

Atmos. Meas. Tech. Discuss., https://doi.org/10.5194/amt-2017-251
Manuscript under review for journal Atmos. Meas. Tech.
Discussion started: 7 August 2017

Atmospheric Measurement Techniques Discussions

Table 2 The statistics of land and ocean AOD comparisons between AERONET/SONET and satellite products as shown in Figure 3.

Satellite AOD algorithm	N	*R*	*MB*	*f* within EE_{DT}	*RMSE*
Land AOD comparison with AERONET					
GOCI YAER V1 all QA	47850	0.86	−0.01509	0.49	0.24
GOCI YAER V1 QA3	38183	0.92	−0.06581	0.49	0.18
GOCI YAER V2	45818	0.91	0.01947	0.60	0.16
MODIS DT	3228	0.92	0.042744	0.62	0.18
MODIS DB	3463	0.93	0.007057	0.73	0.16
Land AOD comparison with SONET					
GOCI YAER V1 all QA	12974	0.83	−0.04817	0.45	0.29
GOCI YAER V1 QA3	10483	0.88	−0.1034	0.42	0.27
GOCI YAER V2	12345	0.85	−0.00668	0.52	0.24
MODIS DT	733	0.82	0.104176	0.46	0.29
MODIS DB	1258	0.86	3.22E−05	0.67	0.27
Ocean AOD comparison with AERONET					
GOCI YAER V1 all QA	19945	0.83	0.056303	0.55	0.17
GOCI YAER V1 QA3	18308	0.88	0.042779	0.62	0.13
GOCI YAER V2	18588	0.89	0.008028	0.71	0.11
MODIS DT	680	0.92	0.033227	0.73	0.09

Atmos. Meas. Tech. Discuss., https://doi.org/10.5194/amt-2017-251
Manuscript under review for journal Atmos. Meas. Tech.
Discussion started: 7 August 2017

Table 3 The expected errors of MODIS C6, VIIRS EDR, and GOCI over ocean and land. μ_0 and μ are the cosine of solar zenith angle and satellite zenith angle, respectively. τ_A and τ_S are AERONET and satellite AOD, repectively.

Algorithm	Diagnostic expected error (DEE)	Prognostic expected error (PEE)	Reference
Ocean			
MODIS DT	Linear regression with bias consideration : $-0.10\tau_A - 0.02$ (lower bound) and $0.10\tau_A + 0.04$ (upper bound)		Levy et al. (2013)
VIIRS EDR	Linear regression with bias consideration : $-0.238\tau_A + 0.01$ (lower bound) and $0.194\tau_A + 0.048$ (upper bound)	Linear regression: $\pm(0.25\tau_s + 0.009)$	Huang et al. (2016)
GOCI YAER V2	Linear regression: $\pm(0.183\tau_A + 0.037)$	Linear regression: $\pm(0.206\tau_s + 0.03)$ Different regression per AOD range: Table 4	This study
Land			
MODIS DT	Linear regression:$\pm(0.15\ \tau_A + 0.05)$		Levy et al. (2010)
MODIS DB	Linear regression: $\pm(0.20\tau_A + 0.05)$	Linear regression with air mass factor consideration : $\pm(0.56 + 0.086)/(1/\mu_0 + 1/\mu)$	Sayer et al. (2013)
VIIRS EDR	Linear regression with bias consideration : $-0.470\tau_A - 0.01$ (lower bound) and $-0.0058\tau_A$+0.09 (upper bound)	Linear regression: $\pm(0.34\tau_s + 0.023)$	Huang et al. (2016)
GOCI YAER V2	Linear regression: $\pm(0.135\tau_A + 0.075)$	Linear regression: $\pm(0.192\tau_S + 0.06)$ Different regression per AOD range: Table 4	This study

Table 4 Prognostic expected error (PEE) estimation of GOCI YAER V2 AOD according to AOD range. The minimum PEE is represented as "noise floor".

GOCI AOD range	Ocean algorithm	Land algorithm
"noise floor"	0.044	0.048
$-0.05 \le \tau_G < 0.50$	$0.07 - 0.59\tau_G + 4.40\tau_G^2 - 10.36\tau_G^3 + 10.64\tau_G^4 - 3.76\tau_G^5$	$0.11 - 1.28\tau_G + 9.81\tau_G^2 - 27.75\tau_G^3 + 37.72\tau_G^4 - 19.86\tau_G^5$
$\tau_G \ge 0.70$	$-0.01 + 0.27\tau_G$	$0.14 + 0.12\tau_G$
$0.50 \le \tau_G < 0.70$	Higher one between two fitting equations	Higher one between two fitting equations

Atmos. Meas. Tech. Discuss., https://doi.org/10.5194/amt-2017-251
Manuscript under review for journal Atmos. Meas. Tech.
Discussion started: 7 August 2017

Figures

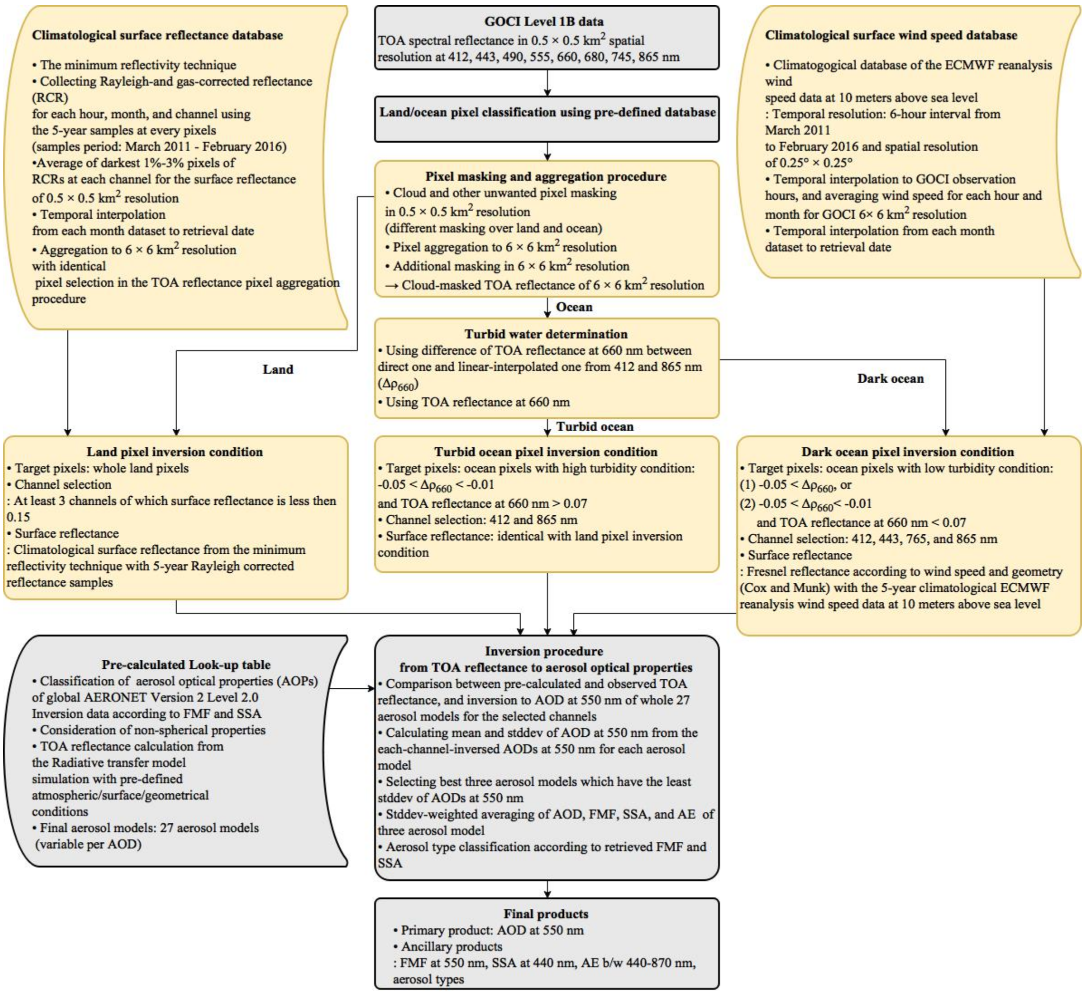

Figure 1 Flow chart of the GOCI Yonsei aerosol retrieval version 2 algorithm. Yellow-colored parts are improved from version 1 to version 2, and gray-colored parts are identical with version 1.

5

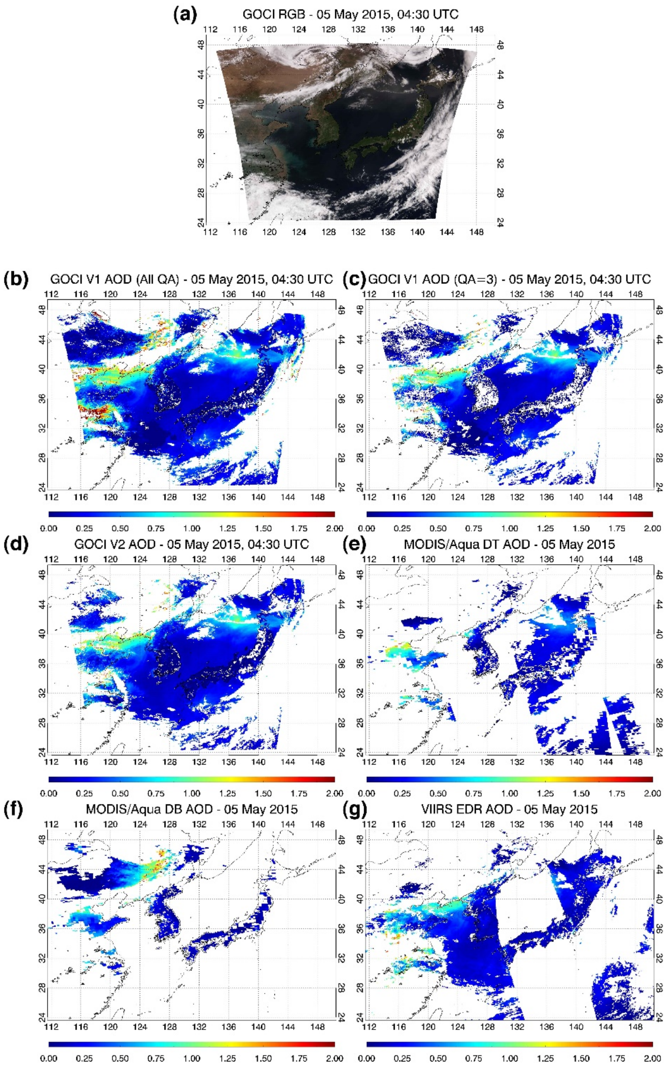

Figure 2 GOCI RGB image and AOD images of GOCI V1 all QA, GOCI V1 QA3, GOCI V2, MODIS/Aqua DT, MODIS/Aqua DB, and VIIRS EDR algorithms in 05 May 2015 over North-East Asia.

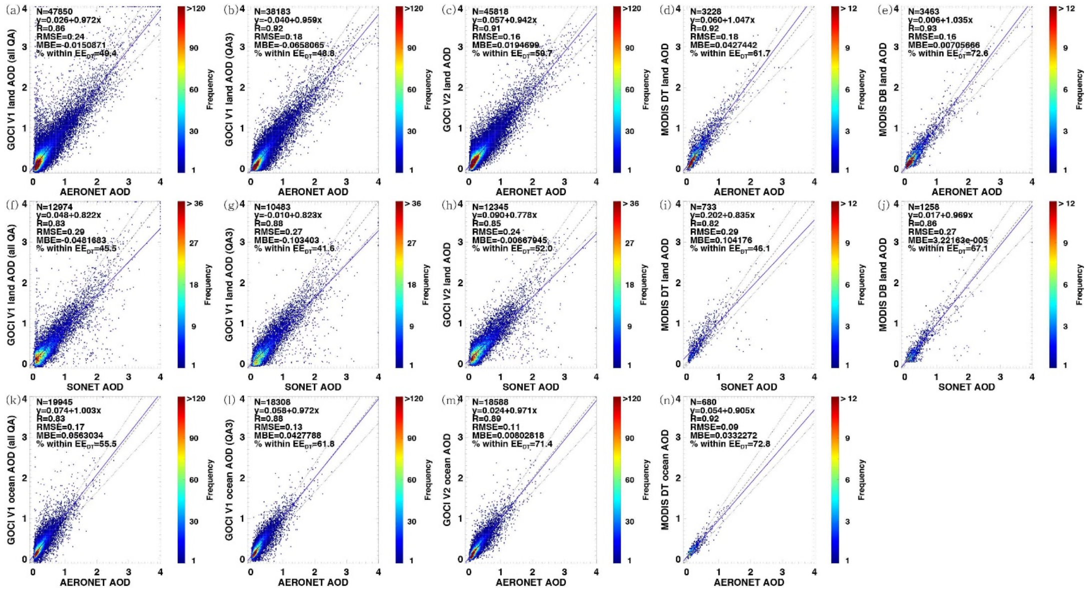

Figure 3 Comparison of AOD between AERONET/SONET and GOCI/MODIS DT/MODIS DB over land and ocean. Variables of x-axis are land AERONET AOD, land SONET AOD, and ocean AERONET AOD from top to bottom, respectively. Variables of y-axis are GOCI YAER V1 for all QA, GOCI YAER V1 for QA of 3 only, GOCI YAER V2, MODIS DT, and MODIS DB from left to right, respectively. Colored pixels represent a bin size of 0.02. Black dashed line denotes the one-to-one line and dotted lines denote the expected error range of MODIS DT AOD.

Atmos. Meas. Tech. Discuss., https://doi.org/10.5194/amt-2017-251
Manuscript under review for journal Atmos. Meas. Tech.
Discussion started: 7 August 2017

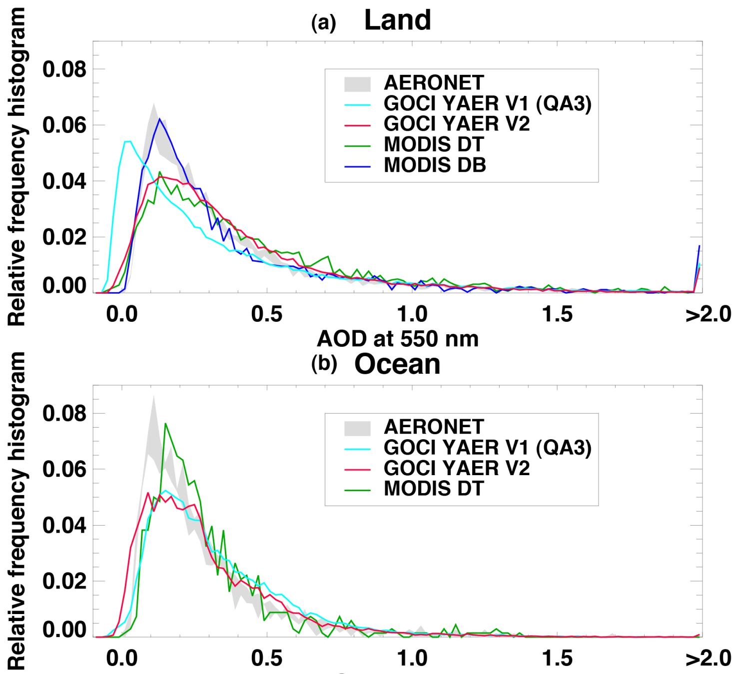

Figure 4 Relative frequency histograms of retrieved AOD from AERONET and satellites over (a) land and (b) ocean.

Atmos. Meas. Tech. Discuss., https://doi.org/10.5194/amt-2017-251
Manuscript under review for journal Atmos. Meas. Tech.
Discussion started: 7 August 2017

Atmospheric Measurement Techniques
Discussions

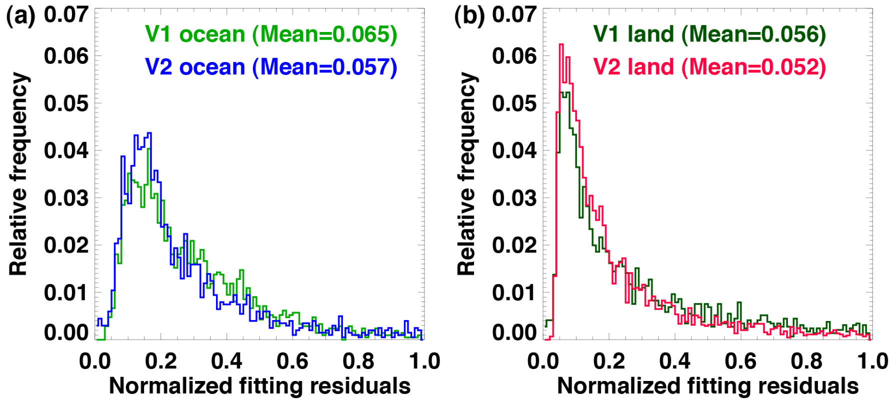

Figure 5 Histogram of normalized fitting residuals of retrieved (a)ocean and (b) land AOD with V1 of QA3 and V2, respectively.

Atmos. Meas. Tech. Discuss., https://doi.org/10.5194/amt-2017-251
Manuscript under review for journal Atmos. Meas. Tech.
Discussion started: 7 August 2017

Atmospheric Measurement Techniques Discussions

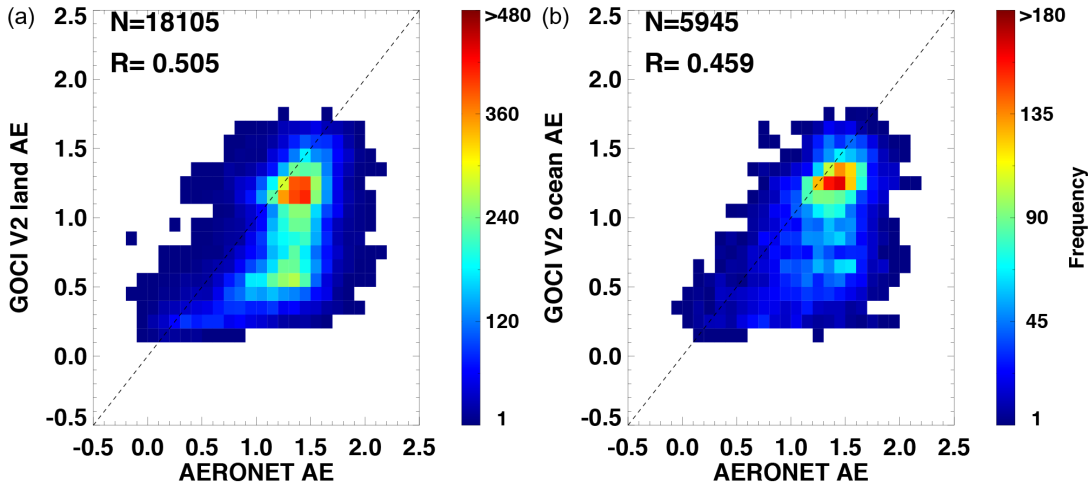

Figure 6 AE comparison between AERONET and GOCI YAER V2 over (a) land and (b) ocean only for AERONET AOD > 0.3. Each colored pixel represents a bin size of 0.10. Black dashed line denotes the one-to-one line.

Atmos. Meas. Tech. Discuss., https://doi.org/10.5194/amt-2017-251
Manuscript under review for journal Atmos. Meas. Tech.
Discussion started: 7 August 2017

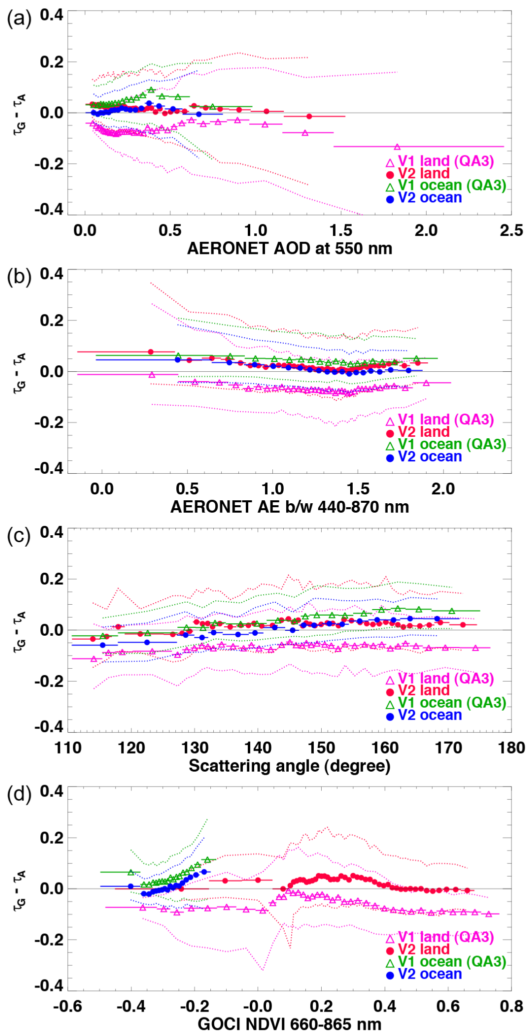

Figure 7 The difference of GOCI and AERONET AOD according to (a) AERONET AOD, (b) AERONET AE, (c) scattering angle, and (d) GOCI NDVI. Each point represents the 50th percentile of each 1000 collocated data sorted in ascending order of each *x*-axis value. Under and upper dotted lines represent the 16th and 86th percentiles range of each point, respectively. Horizontal line of each point represents the range of collocated *x* axis variable.

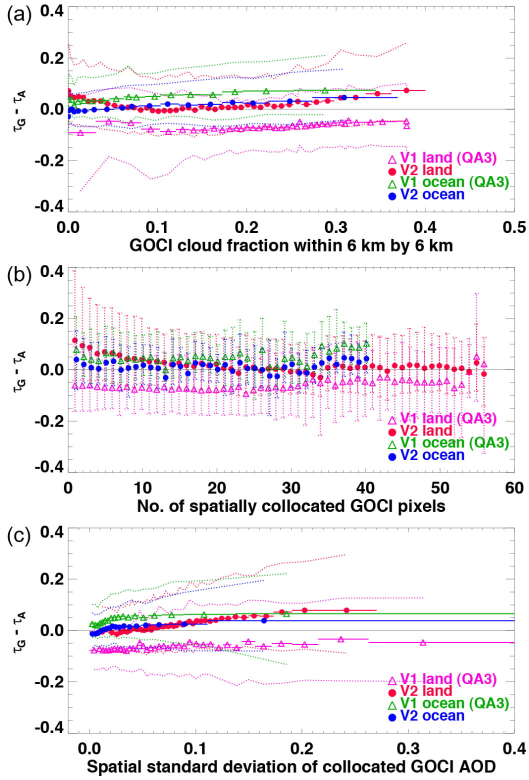

Figure 8 The difference of GOCI and AERONET AOD according to (a) GOCI cloud fraction within aerosol product pixel size (6 × 6 km^2), (b) the number of spatially collocated GOCI pixels within 25 km distance from AERONET site, and (c) spatial standard deviation of collocated GOCI AOD. The points, dotted lines, and horizontal line in (a) and (c) are defined identically with Figure 7. The points and vertical whiskers lines in (b) represent the 50th percentile and 16th-84th range of collocated data corresponding to *x*-axis data.

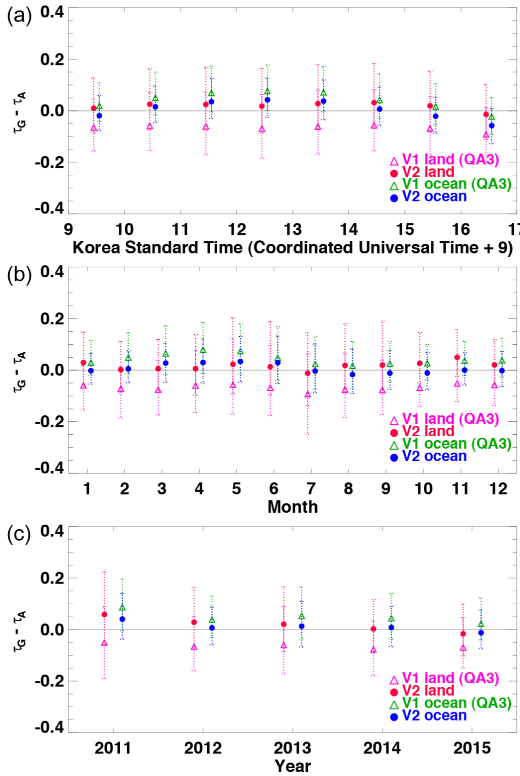

Figure 9 The difference of GOCI and AERONET AOD according to local observation time, month and year. The points and vertical whiskers lines are identical are defined identically with Figure 8(b). Each point is shifted along *x*-axis slightly for better viewing.

Atmos. Meas. Tech. Discuss., https://doi.org/10.5194/amt-2017-251
Manuscript under review for journal Atmos. Meas. Tech.
Discussion started: 7 August 2017

Atmospheric Measurement Techniques
Discussions

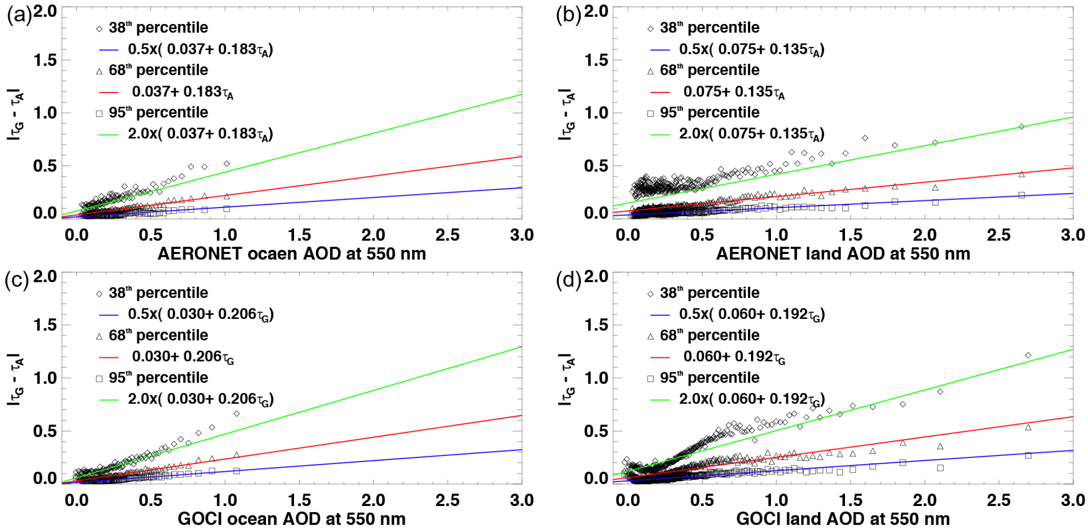

Figure 10 The absolute difference between GOCI YAER V2 AOD and AERONET AOD according to (a) AERONET ocean AOD, (b) AERONET land AOD, (c) GOCI YAER V2 ocean AOD, and (d) GOCI YAER V2 land AOD. The diamond, triangle, and square symbols represent the 38th, 68th, and 95th percentiles of 200 collocated data sorted in ascending order of *x*-axis value, respectively. In (a)-(d), the red line of each panel is the linear least squares fit of the 68th percentiles, and the blue and green lines are the half and double of the red line, respectively.

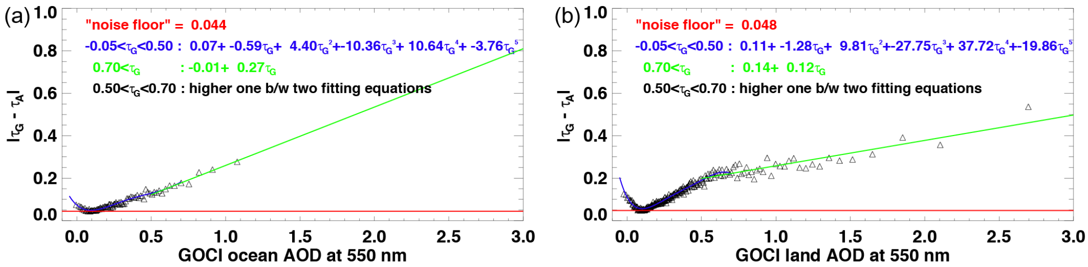

Figure 11 The absolute difference between GOCI YAER V2 AOD and AERONET AOD according to (a) GOCI YAER V2 ocean AOD, and (b) GOCI YAER V2 land AOD, respectively. The triangle symbols represent the 68th percentiles of 200 collocated data sorted in ascending order of *x*-axis value, respectively.

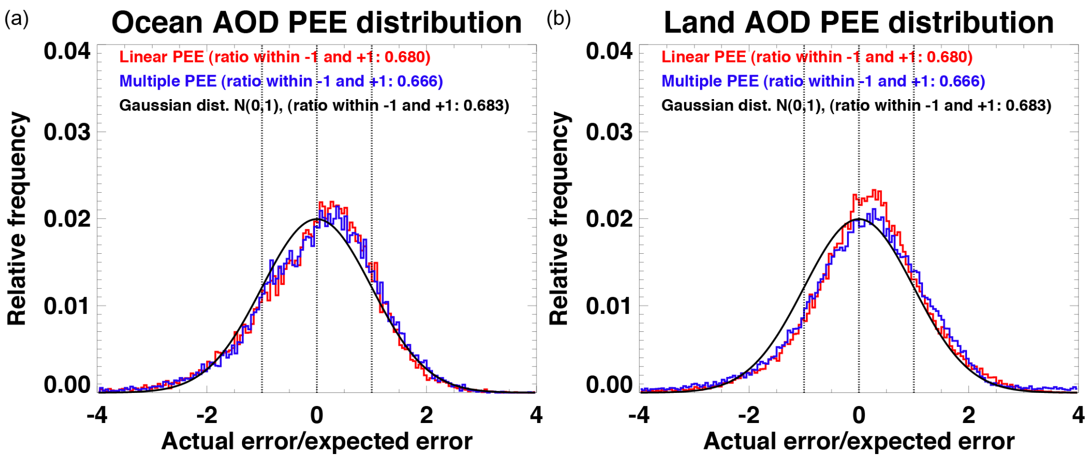

Figure 12 Comparison of observed (a) ocean and (b) land AOD error distribution with theoretical Gaussian distribution for the linear PEE (red) and multiple PEE (blue).

Atmos. Meas. Tech. Discuss., https://doi.org/10.5194/amt-2017-251
Manuscript under review for journal Atmos. Meas. Tech.
Discussion started: 7 August 2017

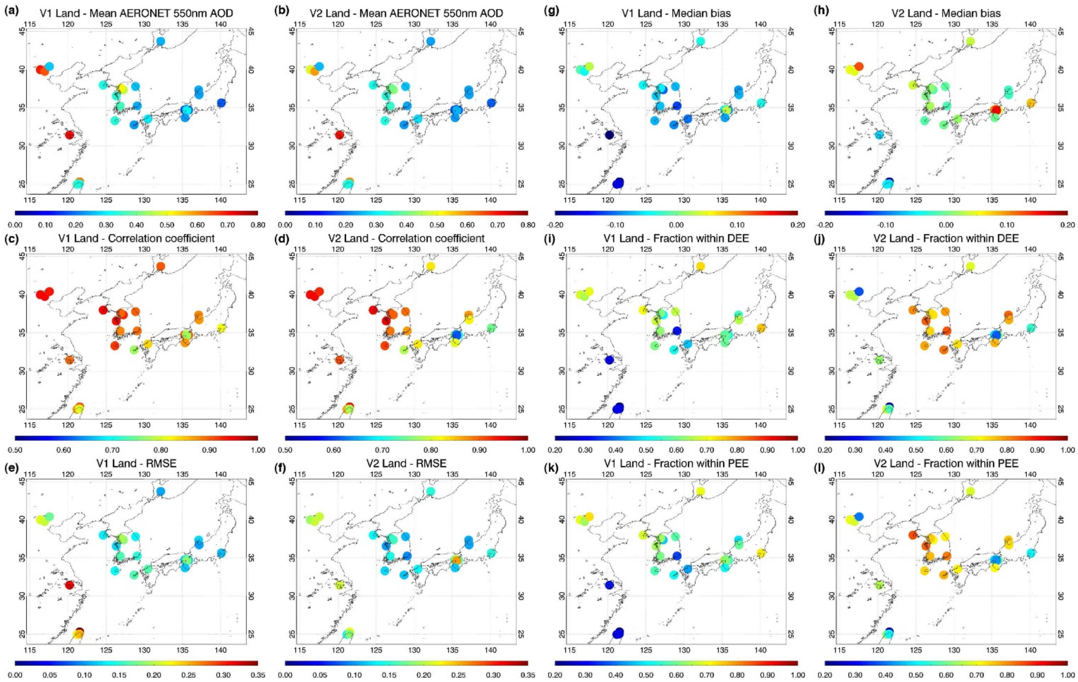

Figure 13 Spatial distribution of statistical evaluation metrics for GOCI YAER V1 QA3 land AOD (1st and 3rd columns) and V2 land AOD (2nd and 4th columns). Left panels indicate mean AERONET AOD, correlation coefficient, and RMSE from top to bottom, respectively. Right panels indicate median bias, fraction within DEE, and fraction within multiple PEE from top to bottom, respectively.

Atmos. Meas. Tech. Discuss., https://doi.org/10.5194/amt-2017-251
Manuscript under review for journal Atmos. Meas. Tech.
Discussion started: 7 August 2017

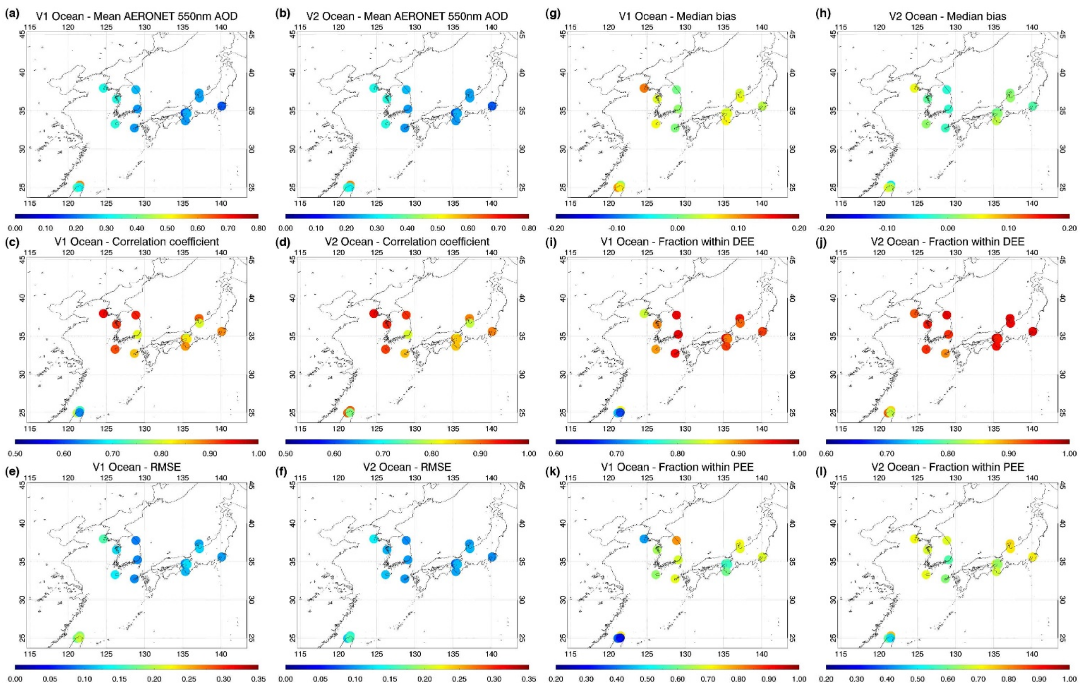

Figure 14 As Figure 13 except for GOCI ocean AOD.